HIGH SPEED LASER DIAGNOSTICS FOR BIOAGENT DEFEAT APPLICATIONS

A Thesis

Submitted to the Faculty

of

Purdue University

by

Alex D. Brown

In Partial Fulfillment of the

Requirements for the Degree

of

Master of Science

December 2019

Purdue University

West Lafayette, Indiana

THE PURDUE UNIVERSITY GRADUATE SCHOOL
STATEMENT OF THESIS APPROVAL

Dr. Steven F.Son, Chair

 School of Mechanical Engineering

Dr. Terrence R. Meyer

 School of Mechanical Engineering

Dr. Emre Gunduz

 School of Mechanical Engineering

Approved by:

 Dr. Nicole Key

  Head of the School Graduate Program

This thesis is dedicated to my family, whose support has meant everything.

ACKNOWLEDGMENTS

First of all, I owe all my experiences working at Zucrow Labs to my advisors Dr. Meyer and Dr. Son. Their mentorship has been invaluable to a new graduate student arriving with no experience in laser diagnostics or energetic materials.

I would like to thank all the fellow graduate students at Zucrow Labs who played a part in my Master's career. Your friendship and technical knowledge have been much appreciated over the past two years. Of particular help, and members of the Fireballs team, were Zach Ayers, Amanda Braun, Mateo Gomez, Daniel Lauriola, Josh Ludwigsen, and Garrett Mathews.

Appreciation is also due to Dr. Mikhail Slipchenko, whose pulse burst laser knowledge was invaluable.

I would also like to thank Dr. Christopher Goldenstein for his technical inputs throughout my work on the Fireballs project, especially in the area of spectroscopy.

TABLE OF CONTENTS

LIST OF FIGURES

ABSTRACT

Brown, Alex D. M.S., Purdue University, December 2019. High Speed Laser Diagnostics for Bioagent Defeat Applications. Major Professors: Steven F. Son, Terrence R. Meyer.

Recent interest in tailoring energetic materials designed to combat biological weapons agents (BWAs) has resulted in significant effort to produce and test these munitions. These energetic materials may contain agent defeat additives that enhance the capability of a munition to destroy BWAs through chemical methods in addition to heat. However, quantifying levels of agent and biocidal species and their interaction is difficult, and efforts have primarily focused on either ex-situ culturing of exposed bioagent simulants or in situ laser absorption measurements. These experiments are valuable for exploring long term agent defeat and line of sight averaged defeat. What these experiments do not provide, however, is in-situ, spatio-temporally resolved imaging in the reaction zone. To address this gap, this work develops the use of in-situ, high speed, two-dimensional optical diagnostics of fireballs and biological weapons agents simulants (BWA-S).

Planar laser induced fluorescence (PLIF) and laser scattering have been conducted in situ. PLIF of both iodine vapor and BWA-S has demonstrated the ability to qualitatively observe species concentration in fireballs. The application of simultaneous techniques provides imaging of multiple parameters, which is invaluable to the further study of BWA-S and agent defeat interactions. These studies also provide the framework for future work in moving towards quantitative measurements, including the development of absorption and fluorescence models.

1. INTRODUCTION

1.1   Background and Motivation

The use of infectious biological weapons dates to at least the Middle Ages. Gabriel De Mussis recorded the 1346 CE siege of Caffa in modern day Ukraine by which the Tatars catapulted their own plague victims into the city, spreading plague and breaking the siege. The further spread of this plague may be the origin of the Black Death which killed millions of Europeans. Since then, biological warfare has been widespread, with notable examples including the deliberate infections of North American indigenous peoples and Japanese biological weapon experimentation in China during World War II. In more recent memory, Saddam Hussein possessed weapons containing botulinum toxin, anthrax, and aflatoxin during the Persian Gulf War, although they were unused [1].

Biological weapons are also used by private individuals or groups engaging in biocrime and bioterrorism. Bioterrorism is the use of biological agents to create widespread fear, disruption, and casualties. Examples can be seen following the events of September 11 where letters containing anthrax were used to infect multiple people, and in 1984, when 751 people in The Dalles, Oregon were infected with salmonella bacteria in attempt by the Bhagwan Shree Ragneesh cult to control local politics. Biocrime is the directed use of biological agents to infect low numbers of people or individuals. For example, in 1978 the KGB is believed to have murdered the Hungarian Georgi Markov with ricin pellets to silence his criticism of the Bulgarian government. Appendix A contains a chart from Jansen et al. that describes multiple biological weapons that have shown potential for bioterrorism [2]. Combined with such estimates that 100 kg of aerosolized anthrax spores released in the Washington

DC area could cause up to 3 million deaths, it is clear that methods to counteract BWAs are necessary [3].

Methods used to destroy or inactivate BWAs include heat, ultraviolet light exposure, and chemical exposure, among others [4]. Traditional munitions would rely upon heat exposure as the primary mode of inactivation of BWAs. However, in a report by May and Haldeman, it was theorized that a nuclear weapon of 1 to 10 kilotons delivered into an underground bunker containing stores of BWAs would likely only sterilize all bioagents within a 10-30 meter radius, and potentially disperse any surviving agents into the atmosphere [5]. In addition, some weapons are composed of bacterial spores, dormant bacteria with a protective shell of peptidogylcan. These spores are known to be resistant to high temperatures, particularly dry heat [6].

In order to increase the effectiveness of a weapon to destroy BWAs, it is therefore desirable to enhance the thermal destruction of bioagents with another aforementioned method. Recently there has been significant effort within the energetics community to generate formulations that produce biocidal species. Certain gaseous molecules such as iodine are known as biocides [7]. Tailoring a munition that contains these species as a key combustion product would theoretically increase the ability to destroy BWAs.

The objective of this work is to develop high-speed, in-situ measurement and imaging techniques for evaluating the diatomic I_2 produced by a reacting energetic material. A biological weapons agent simulant (BWA-S) was also tested to determine if in-situ destruction could be imaged. Techniques tested were planar laser-induced fluorescence (PLIF), laser scattering, and high speed imaging. A spectroscopic absorption model for I_2 was also developed.

2. I_2 CHARACTERISTICS, ENERGETIC FORMULATIONS, AND BIOCIDAL EFFECTS

2.1 I_2 as a Biocidal Additive to Munitions

As a halogen, diatomic iodine (I_2) is an effective bactericidal and sporicidal agent [7]. I_2 is highly reactive and acts as a strong oxidizing agent, although it is the weakest oxidizer of the halogens. I_2 will sublime at ambient temperature and pressure, and as a result long term stability is a significant issue when working with I_2. Solid I_2 has a melting point at 113.7 °C and will boil at 184 °C [8]. There are two major strategies for adding I_2 to energetic materials. The first is to stabilize I_2 within a metal or metalloid fuel matrix, typically aluminum (Al), magnesium (Mg), or boron (B). The second is to incorporate an oxidizer such as I_2O_5 into a thermite formulation [9]. Recent advances in the production and testing of each will be discussed briefly here.

As I_2 is relatively unstable, significant effort has been made to stabilize I_2 complexes in metal fuels. Zhang et al. discovered that varying forms of I_2 could be produced in an aluminum matrix by mechanically milling I_2 and aluminum, producing elemental I_2, AlI_3, and a third form that was found to release at temperatures of 500-600 °C [10]. Zhang later improved the method and found that 20 wt. % of I_2 could be retained through mechanically milling samples for 25 hours, although the addition of I_2 lowered ignition temperatures compared to pure Al. It was theorized that the retention of more than 20 wt. % I_2 may be unfeasible [11]. Abraham et al. found that ternary compositions containing Al, B, and I_2 could be mechanically milled to retain 20 wt. % of I_2 and release I_2 at higher temperatures than the I_2 boiling point, which is desirable in terms of long term storage [12]. A similar study by Wang et al. using Mg, B, and I_2 was found to be similarly stable with 20 wt %

I_2 [13]. C_2I_4 and SnI_2 were found by Johnson et al. to release significant amounts of gaseous I_2 upon combustion when combined with various thermites [14].

Other work has focused on attempting to create I_2 containing energetic formulations such as thermites. Producing a stable I_2 thermite is desirable, as many thermites are highly exothermic and may result in significant I_2 production. This potentially could lead to a munition that combines a high likelihood of heat defeat of biological weapons with iodine's biocidal characteristics. I_2O_5 is a promising oxidizer in that it contains both 76 % mass I_2 and will produce significant amount of I_2 upon reaction. However, I_2O_5 is hygroscopic and will absorb ambient moisture to form HIO_3, which is corrosive to metals, and will also react with Al to form Al_2O_3. This hinders the combustion performance of possible Al-I_2O_5 thermites. Stabilizing I_2O_5 has been researched by recent studies, and notably Feng et al. found that I_2O_5 could be passivated within an Fe_2O_3 shell, and that this composite could form a highly reactive thermite when combined with nanoaluminum (nAl) [15]. Many other fuel-oxidizer formulas are possible, for example, Wang et al. demonstrated the ability to synthesize both Al-$Ca(IO_3)_2$ and B-$Ca(IO_3)_2$ via arrested reactive milling. Both thermites had similar flame temperatures although B-$Ca(IO_3)_2$ had better stability and as a result shows better promise for biocidal munition creation [16].

2.2   Biocidal Effects of I_2 Containing Energetic Formulations

As there has been much work on synthesizing energetic I_2 compounds, also much study has focused on the effects of exposing bacterial and viral species to the combustion product of these compounds. Clark et al. exposed solutions of Bacillus atrophaeus spores to the combustion products of various Al-I_2 thermites: Al-I_2O_5, Al-Fe_2O_3, and Al-Ag_2O. After culturing the bacterial suspensions, it was found that the Al-I_2O_5 resulted in the highest degree of inactivation, more so than the material containing silver, itself a biocidal material [17].

To see the effects of I_2 exposure on aerosolized bacterial spores, Grinshpun et al. passed aerosolized Bacillus atrophaeus spores and MS2 virus coaxially to a flame seeded with varying composites. Al-I_2 composite powder resulted in higher levels of inactivation compared with other compounds without I_2 [18]. To improve the experimental setup, Aly et al. exposed Bacillus atrophaeus spores to the combustion gases of similar composites at various heights above the flame, leading to a better understanding of the dynamic roles of heat and chemical affect on spores. A new ternary composite, Al-B-I_2 was tested, and showed a higher level of defeat than the Al-I_2 tested previously [19].

In a study designed to further explore the relationship between heat and chemical destruction of bacterial spores, Wang et al. exposed bacterial spores to Al/Bi_2O_3 and $Al/Bi(IO_3)_3$ thermite reaction products, and found that the metal iodate thermite resulted in higher levels of defeat as well [9]. To quantify bacterial viability, spores were coated on an aluminum substrate and cultured post situ for analysis.

3. BIOLOGICAL AGENT SIMULANTS AND DIAGNOSTICS

3.1 Biological Agents and Simulants

As laboratory testing with actual biological weapons agents (BWAs) such as anthrax is extremely hazardous, the use of biological weapons simulants (BWA-S) is much preferred for most academic settings. According to Cenciarelli et al., "A BWA-S is a harmless biological agent which mimics the physical and structural properties of a real BWA, without causing any adverse health effects" [20]. In other words, choosing a BWA-S that is morphologically similar to a true BWA is critical to make evaluations of the biological defeat capability of a system.

The major variants of biological weapons are bacterial, bacterial spores, viruses, or toxins. Bacterial weapons can be split further into two major morphological categories: Gram-negative and Gram-positive. Gram-positive bacteria have a surface protein layer that Gram-negative do not, while Gram-negative bacteria feature an additional membrane outside the cell wall that Gram-positive bacteria lack. A common BWA-S for Gram-positive bacterial species such as B. anthracis (anthrax) or c. Botulinum (botulism) is B. Subtilis, which can also serve as a spore substitute. Gram-negative agents include Y. pestis (plague), and accepted simulants are certain non-pathogenic strains of E coli. Spores are typically the result of Gram-positive bacteria undergoing morphological change in response to environmental stresses. Accepted BWA-S include B. atrophaeus, B. subtilis, and B. thuringiensis. Though considered biological agents, toxins are not technically living organisms, rather they are protein structures produced by bacteria. A well-known toxin is Ricinus communis (ricin) and, several BWA-S are Bovine Serum Albumin (BSA) and Ovalbumin (OA), both animal proteins, and are considered safe [20]. For use in this study, albumin

was chosen as both a harmless and readily obtained BWA-S that contained biological fluorophores as discussed below.

3.2 Detection and Diagnostics of Biological Simulants

This section is devoted to a summary of the various optical diagnostic methods used for the detection of airborne BWA-S, which forms the basis for BWA-S experimentation in this work.

Many biological materials will emit fluorescence following ultraviolet (UV) excitation. The main compounds responsible for this phenomena are the amino acids tryptophan, tyrosine, and phenylalanine, the reduced nicotinamide adenine dinucleotides NADH and NADPH, and flavine adenine dinucleotides FAD and FADH. The excitation peaks for the amino acids are 280 nm, 275 nm, and 255 nm, respectively. NADH and NADPH have excitation maxima around 340 nm, while FAD and FADH have excitation peaks near 450 nm [21]. As a result, it is possible to access these excitation wavelengths using ultraviolet lasers and collect the resulting laser induced fluorescence in order to probe BWA-S. Commonly used systems utilize the third and fourth harmonic of Nd:YAG lasers operating at either 355 or 266 nm.

Recently, a large amount of work involving ultraviolet laser induced fluorescence (UV-LIF) has been conducted with the goal of measuring bioaerosols remotely. Kaliszewski et al. reported the construction and testing of a remotely operated bioaerosol detector involving the use of a continuous wave laser operating at 375 nm. The detection components consisted of bandpass filtered photomultiplier tubes capable of measuring different fluorescence bands to distinguish between various bioaerosols. The instrument is capable of sampling ambient bioaerosols and was mounted to a controlled robot in order to operate at distance [22].

Farsund et al. conducted UV-LIF at a standoff distance of 210 m in which both 355 and 294 nm light generated from and Nd:YAG laser were used to probe various bioaerosols. The 294 nm light was generated using an optical parametric oscillator

with the goal of accessing the sub-300 nm excitation spectra of amino acids while avoiding the serious absorption of 266 nm light by atmospheric O_3, which may be up to 90% per kilometer. Emission spectra were successfully collected for 7 BWA-S at the 210 m distance, and it was found that 294 nm excitation resulted in equal or higher fluorescence signal for similar laser pulse energies than 355 nm light [23]. Differences in the fluorescence spectra of each BWA-S were identified, which shows promise for the identification of a cloud of unknown bioaerosols at safe standoff distances. The increase in fluorescence signal, and thus signal-to-noise ratio, at 294 nm may be helpful in isolating distinct features of each BWA-S for high fidelity identification.

The advantages of UV-LIF lie in the fact that fluorescence signal may be collected remotely, as demonstrated by Farsund et al., and that high pulse energies at ultraviolet wavelengths are accessible from commercial high speed Nd:YAG laser sources. High pulse energies are of particular usefulness in conducting tests within fireball environments, as Glumac reported attenuation lengths of 405 nm light in RDX fireballs as short as 5 cm up to 5 ms after initiation. Attenuation length can be defined as the length in a medium by which the amount of travelling light has been reduced to $1/e$, or roughly 37% [24].

4. IODINE SPECTROSCOPY

Spectroscopy of the I_2 molecule is a well studied topic. The information that is relevant to laser induced fluorescence will be included here, but is by no means a comprehensive overview of all the intricacies of I_2 spectroscopy. I_2 possesses a dense absorption structure that occurs in the visible wavelength spectrum. The absorption spectrum of I_2 is shown in Figure 4.1 [25]. This absorption structure is the result of the $X^1\Sigma_g^+$ - $B^3\Pi_{0+u}$ electronic transition. The potential energy diagram for this transition is shown in Figure 4.2 [26]. The transitions in this system result from electronic transitions from the ground state at various v" vibrational levels to upper v' levels. At room temperature, approximately 98.4% of iodine molecules are in the v"=0-3 states, per the author's Boltzmann calculations included in Appendix B.

4.1 The $X^1\Sigma_g^+$ - $B^3\Pi_{0+u}$ Transition

The $X^1\Sigma_g^+$ - $B^3\Pi_{0+u}$ electronic transition is interesting in that the electronic spin terms are different. In the molecular term symbol, $^{2S+1}\Lambda_\Omega$, S represents electronic spin. Therefore for the X state the electronic spin term S is equal to 0 and in the B state is equal to one. As a result, the transition is only weakly allowed. This leads to I_2 having a characteristically long radiative lifetime following excitation [25]. In a study by Sakurai et al., the collision-free radiative lifetime of I_2 was measured for the $X^1\Sigma_g^+$ - $B^3\Pi_{0+u}$ transition for vibrational transitions from v"=0 to v'= 3-25, occurring at wavelengths from 621.4 nm to 546.2 nm. The lifetimes ranged from 530 ns to 1.59 μs [27]. In a similar study, the radiative lifetime of I_2 excited at 532 nm for the reported v"=0 to v'=32 transition, similar to the wavelength used in this study, was found to be 1.05 μs [28]. However, as reported by Sakurai et al., the radiative lifetime of I_2 is coupled with the v' level. This was conjectured due to the
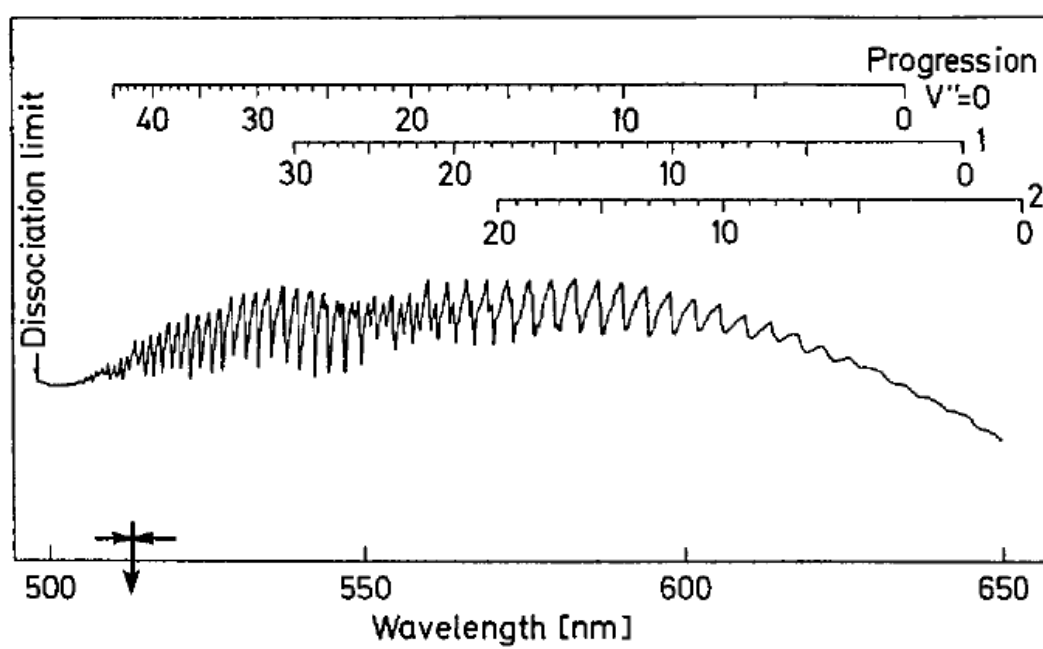
Fig. 4.1. Visible Absorption Spectrum of I_2 [25]
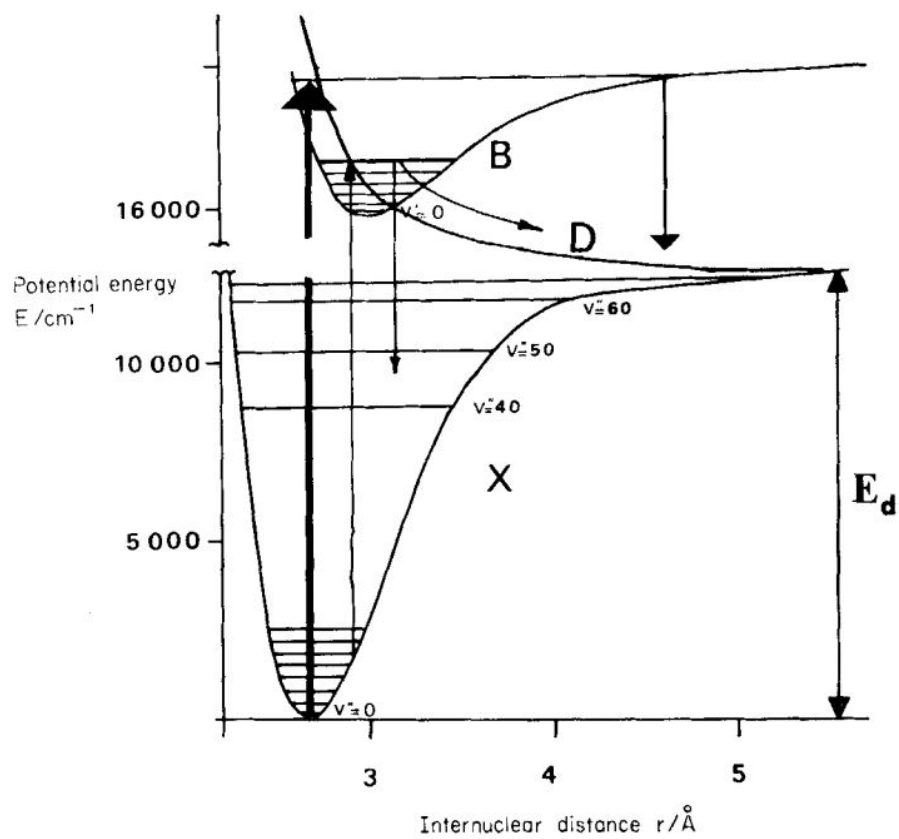
Fig. 4.2. Potential Energy Curve of I_2 [26]
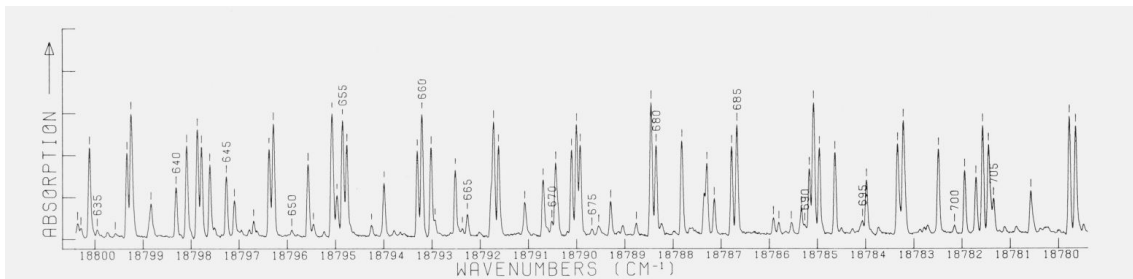
Fig. 4.3. Iodine Absorption Spectrum from 18780 cm^{-1} to 18800 cm^{-1}

fact that the lifetime was variable with constant foreign gas quenching and [27]. The result in [28] cannot be taken to be exact to the I$_2$ transitions used in this paper, as the accessible transitions to a frequency doubled Nd:YAG laser operating at 532 nm will cover multiple vibrational and many rotational levels. Figure 4.3 shows the absorption spectrum of a portion of the visible light spectrum, from 18780 cm^{-1} to 18800 cm^{-1}, or about 531.91 nm to 532.48 nm [29]. Within this short span there are 76 distinct lines, and many of these lines are comprised of multiple overlaid vibrational and rotational transitions.

4.2 Dissociation

Another issue encountered within I$_2$ absorption and emission spectroscopy is the prevalence of both direct dissociation and predissociation. Predissociation is the dissociation of a molecule in an excited electronic state through internal mechanisms [30]. Predissociation is not equivalent to photodissociation, which is direct dissociation following the absorption of a photon. In the case of I$_2$, predissociation occurs from the $B^3\Pi_{0+u}$ state to the "D" state in Figure 4.2. In a study by Brewer and Tellinghuisen, the quantum yield of the excitation and relaxation to and from the $B^3\Pi_{0+u}$ state was evaluated. Many vibrational transitions were studied, including the transition at 527.7 nm, which is relatively close to 532 nm, and will be given as an example here. It was found that 83% of absorbed light resulted in discrete excitation to the $B^3\Pi_{0+u}$ state, while 17% is continuum absorption into an alternate state. Of the 83%

light absorption into the electronic state of interest, 59% of the excited molecules pre-dissociate, and 41% fluoresce [31]. Therefore, for this transition, only about 49% of absorbed light is seen as fluorescence. This is of interest for fluorescence experiments as dissociation will limit the efficiency of a measurement. This also contributes to the radiative lifetime of the excited state of I_2, which must be accounted for when designing a fluorescence experiment.

4.3   Quenching

The rate at which I_2 is collisionally quenched will play a role in the fluorescence lifetime of the excited $B^3\Pi_{0+u}$ state. This can occur through two pathways: the collision of an excited I_2 molecule with another I_2 molecule or the collision of an excited I_2 molecule with a foreign gas species. Figure 4.4 shows the two level model, a simplified model for absorption and fluorescence taken from [32]. In reality, I_2 absorption and fluorescence is much more complex, with many absorption lines being accessed by even a narrow laser line, and with fluorescence resulting from the decay to multiple ground state vibrational levels. This is the reason for many distinct peaks in the I_2 fluorescence spectrum. However, the two level model serves to visualize the different processes occurring during absorption and fluorescence.

Collisional quenching is the term labelled $n_2 Q_{21}$. n_2 is the population density of excited molecules, and Q_{21} is the rate of collisions that result in de-excitation. Q_{21} is dependent on the number density of quenching molecules, temperature, and the quenching cross section of the quenching molecule with I_2. In general, I_2 is a very effective self-quencher, with quenching cross sections generally reported to be around 64 Angstroms [25, 27, 28]. For reference, Masiello et al. reported quenching cross sections of N_2, O_2, and CO_2 with I_2 as 2.89, 3.54, and 12.1 Angstroms respectively.

In the case of I_2 PLIF conducted in reacting environments, quenching poses multiple problems. The higher the I_2 population, the more it will self-quench, as evidenced by the strong quenching cross section of I_2 with itself. Also, the populations of for-
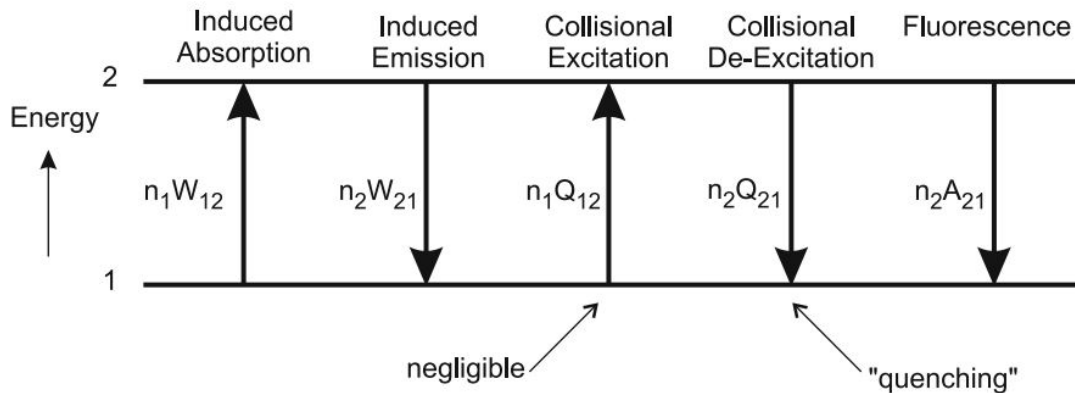
Fig. 4.4. Two level model for absorption and fluorescence [32].

eign gases at any time within a transient reacting environment, such as a fireball, are difficult to predict. It is possible that the main source of I_2 collisional quenching is due to I_2 itself.

Bernecker et al. studied the combustion products of HMX at various pressures using mass spectrometry. Experimentally, it was found that HMX powder at atmospheric pressure produced mole fractions of 33.19, 23.79, 22.83, 9.82, and 9.15 for N_2, CO, H_2O, CO_2, and H_2 [33]. Assuming that the presence of I_2 does not appreciably affect the gaseous reaction products of HMX, it is clear that I_2 self quenching will dominate for high concentrations of I_2 in an HMX fireball with 50% loading of I_2 as was used in this study.

4.4 I_2 Modelling

Effort was made to create an I_2 absorption and fluorescence model in order to inform experimentation and to evaluate theory. The model also has the goal of moving towards a quantitative I_2 PLIF measurement.

The base of the model is the calculation of Boltzmann fractions for different ground state energy levels. The basics of these calculations are included in Appendix B.

Upon the selection of an excitation wavelength, the relevant Boltzmann fractions can be calculated, such that the available population for excitation at a relevant temperature is known. This is desirable for maximizing signals.

5. EXPERIMENTAL CONFIGURATIONS AND METHODS

5.1 Laser and Camera Systems

The experiments conducted utilized a custom Nd:YAG pulse-burst laser at Purdue University developed by Slipchenko et al. [34]. The characteristic wavelengths that are emitted from the laser are 1064 nm and 532 nm with a bandwidth of less than 2 GHz. The laser was operated at 532 nm for I_2 experiments and was further frequency tripled to 355 nm for BWA-S experiments. The laser is capable of 180 mJ pulse energies at 532 nm at a repetition rate of 20 kHz for a 10.5 ms burst. The laser wavelength could also be changed by altering the input seed laser operating temperature to tune across the fine I_2 absorption spectrum, as shown in Figure 4.3, and access strong absorption lines. Given that the laser bandwidth is roughly 0.0667 cm^{-1}, it is possible to isolate individual lines . For BWA-S, this tuning is less important as the absorption spectrum is broad. The laser could be externally triggered to provide measurement points at precise times within a fireball event.

A variety of high-speed cameras and image intensifiers were used throughout the experimental testing. For spectra, a Princeton Instruments Acton Series SP 2500 spectrometer was used with an Andor Newton EMCCD camera. For high speed imaging, the cameras used were Phantom v2012 high speed cameras and Photron Fastcam SA-Z cameras. The image intensifiers used were Lambert HiCATT and LaVision IRO units. The LaVision IRO had a UV-enhanced photocathode for increased detection in the UV wavelengths, useful for the BWA-S experiments. The image intensifiers were coupled to the high-speed cameras and timed to synchronize with laser pulses such that the laser pulse would be captured by the short intensifier gate. Typically, the gate of the intensifier was the limiting exposure setting. In this way, the cameras

could be left to expose for the maximum time at the recording frame rate but only collect signal from the shorter time gate of the intensifier. By using a photodiode to monitor laser pulses, it was possible to precisely time the intensifier gating to the laser pulses, which was necessary to reduce the intensifier gating as much as possible to eliminate flame emission from inflating the measurements. A variety of optical bandpass filters were used to collect the desired emission from each experiment.

5.2   Energetic Formulations and Charge Characteristics

Charges were composed primarily of HMX and I_2, with aluminum added for some experiments. HMX is a high explosive commonly used in military applications, and was chosen as a base material due to its widespread use. I_2 crystals were purchased from Sigma Aldrich and were ground prior to mixing with HMX. Aluminum was added to increase the energy release of the charges, but aluminum is known to greatly increase the optical depth of fireballs, making laser measurements more difficult [35].

Charges were prepared immediately prior to testing. HMX was stored in an oven and removed for charge preparation to reduce the absorption of ambient water. Ground I_2 crystals were added to HMX at this time to reduce the effects of aging. The charge composition was placed in a small 3D printed holder with a 1.6 cm^3 cylindrical cavity to hold the charge. The 3D printed holder had a small entry port for inserting an electric match, purchased from J-Tek. The electric matches used were coated in a proprietary pyrogen mixture, which was ignited with a pulse from a capacitor discharge unit (CDU). The CDU used was a Teledyne Risi FS-43 firing unit. This unit was typically charged to 3.5 kV and then discharged to ignite the electric match, which would then ignite the HMX and I_2 mixture. The CDU unit is capable of firing upon reception of a trigger signal, and could also output a trigger signal. These features were used to precisely time the laser and camera systems to probe different times in a fireball event. Figure 5.1 shows a typical fireball produced by these charges, and Figure 5.2 shows the visible flame emission integrated across the
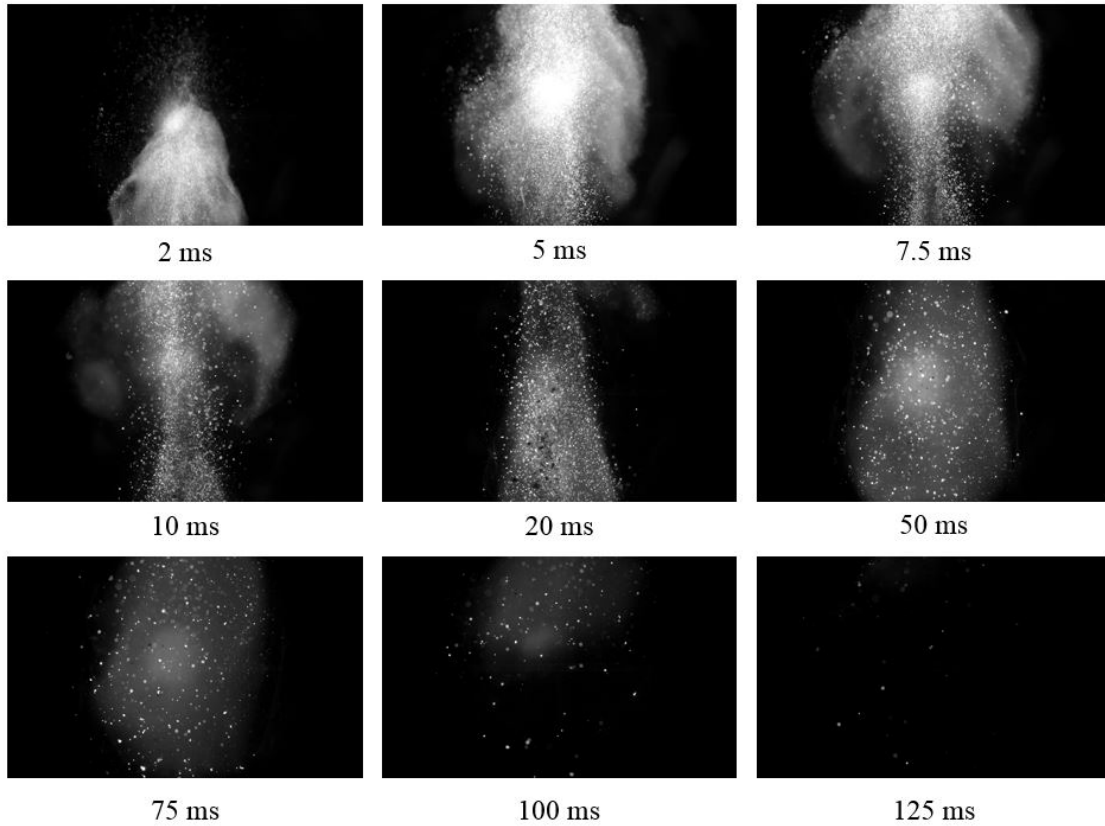
Fig. 5.1. A characteristic fireball from a charge consisting of 150 mg HMX and 50 mg ground I_2. The visible flame emission was captured with a Phantom v2012 camera at 10 kHz, with an exposure of 10 μs and an f-number of 5.6.

whole camera chip against time at a rate of 10 kHz. An intense luminosity peak prior to 20 ms is observed corresponding to the electric match ignition and initial blast, followed by a sustained burning event that lasts past 100 ms. Therefore, measuring I_2 during these times will give some insight as to how I_2 is behaving during the bulk of the strong fireball emission. At times later than this, measurements will show how long I_2 persists in the environment following a charge.
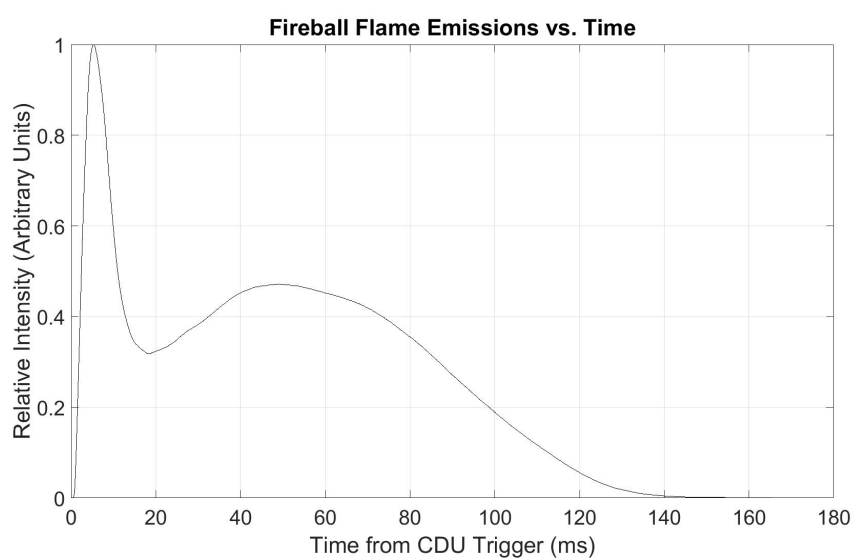
Fig. 5.2. Integrated flame emission plotted against time for a characteristic fireball. Charge composition was 150 mg HMX and 50 mg I_2.

5.3   I$_2$ PLIF

5.3.1   Spectral Acquisition and in Fireballs

In order to effectively reduced the flame emission as seen in Figure 5.2, bandpass filters were chosen to capture a portion of the I$_2$ fluorescence spectra. Spectra were taken by integrating the fluorescence signals resulting from a 10.5 ms 532 nm laser burst through a Thorlabs vapor reference cell containing I$_2$ at a pressure from 0.1 to 1.2 Torr. The Princeton Instruments spectrometer with a grating of 300 grooves/mm was used to image the spectrum onto an Andor Newton EMCCD camera, which integrated the 210 laser pulses in the burst on a single exposure, which allowed for the collection of a spectrum with high signal levels. The laser line and resulting resonant fluorescence at 532 nm can be see even though a 532 nm notch filter with an optical density of 4 was used. The spectrometer was calibrated using Newport pencil-style calibration lamps, which emits known distinct fluorescence peaks within the range of wavelengths shown in Figure 5.3. Using the I$_2$ spectra, multiple bandpass filters that could isolate multiple fluorescence peaks were purchased for use in reactive testing.

A schematic of a testing configuration is shown in Figure 5.4. In general, the 532 nm beam would be expanded in one direction using a cylindrical lens, and then focused to a thin "sheet" using a spherical lens. An intensifier and camera perpendicular to the laser sheet can be used to image the resulting I$_2$ fluorescence using bandpass filters.

5.3.2   I$_2$ Calibrations

A small optical chamber was created to test experimental parameters involving I$_2$ absorption and fluorescence. The chamber was constructed with parts from Kurt J. Lesker and Thorlabs, and consisted of a four way tee with 3 optical windows and a single vacuum flange. Figure 5.5 shows a picture of the chamber, with a
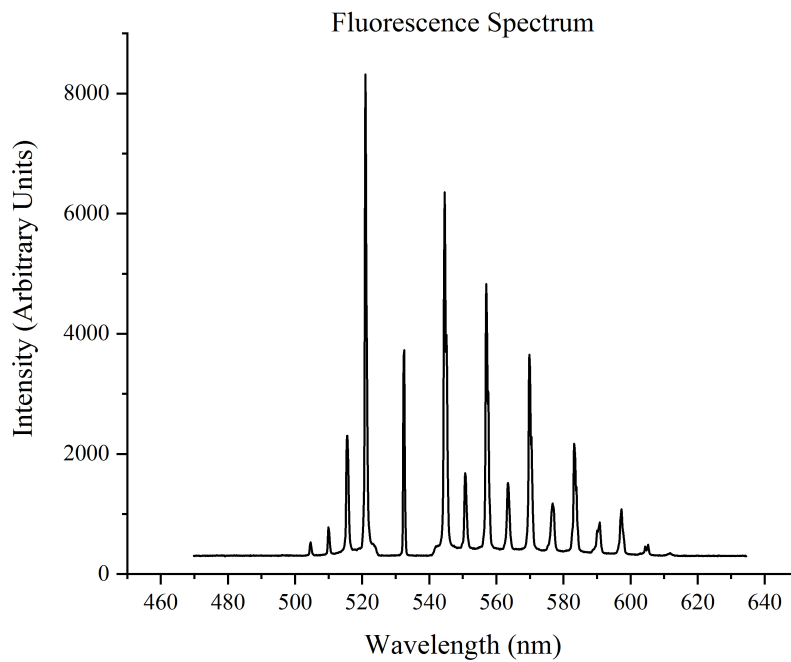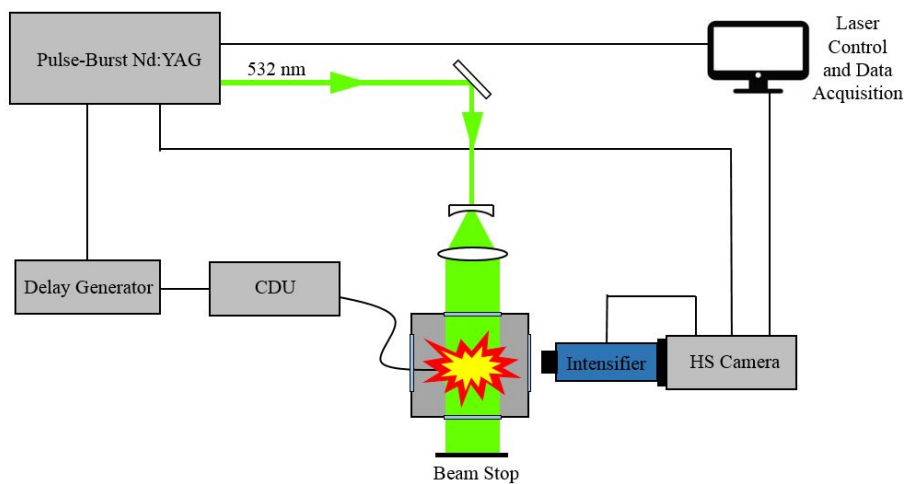
Fig. 5.3. Example I$_2$ fluorescence spectra.

Fig. 5.4. Example schematic for an I$_2$ PLIF experiment in a fireball.

clear line of yellow I_2 fluorescence visible. Green tinting is due to 532 nm laser scattering reaching the camera. The optical windows are AR coated to reduce laser light reflections. The flange on the fourth leg of the tee was drilled with two ports: one for a type-K thermocouple for monitoring gas temperature inside the cell, and another that allowed for the connection of a vacuum pump. I_2 crystals were placed into the chamber, and then the chamber was sealed. The vacuum pump was turned on slowly to avoid disturbing the I_2 crystals. A vacuum gauge was monitored to measure the pressure inside the cell. The advantage of bringing the chamber to a lower pressure was to reduce collision quenching of I_2, increasing the fluorescence signal. During experimentation it was found that gaseous I_2 would condense on the windows, therefore it was necessary to maintain hot air flow onto the windows to keep them at a temperature such that no I_2 would condense.

The evacuated chamber containing I_2 crystals was then heated using heat tape purchased from Omega and controlled with a feedback thermocouple attached to the outside of the chamber. As the internal temperature of the chamber could be monitored with the internal thermocouple, the external temperature was irrelevant. By use of the Clausius-Clapeyron Relation shown in Equation (5.1), the pressure of I_2 gas inside the chamber can be calculated at a given temperature if a valid pressure and temperature, P_1 and T_1 , are known, as well as the heat of vaporization of I_2. Figure 5.6 shows a graph of I_2 vapor pressure calculated using the Clausius-Clapeyron Relation.

$$ln(\frac{P_1}{P_2}) = \frac{\Delta H_{vap}}{R}(\frac{1}{T_2} - \frac{1}{T_1}) \tag{5.1}$$

5.4   Bioagents

For a BWA-S, albumin was chosen, which was previously discussed as benign simulant for a BWA [23]. Albumin was purchased from Carolina Scientific. Initially, albumin was mixed with the explosive charge, however it was found that this resulted

Fig. 5.5. Constructed calibration cell showing I$_2$ fluorescence.
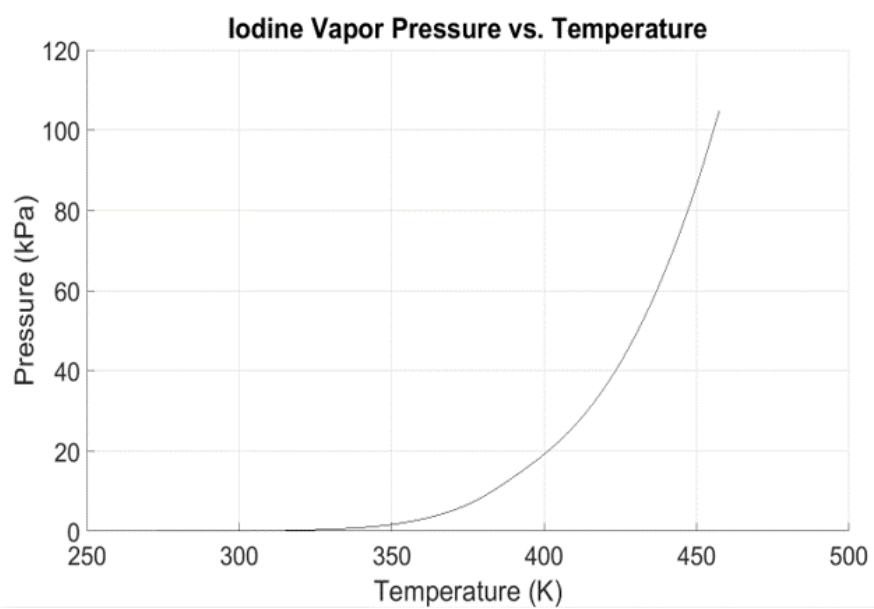
Fig. 5.6. I_2 vapor pressure plotted against temperature using the Clausius Clapeyron Relation

in all the albumin being destroyed as no signal was found using UV-LIF, which is unsurprising given that the albumin was exposed to the maximum temperatures of the fireball. In order to inject BWA-S into a fireball, simulating a potential bioaerosol, a small solenoid valve supplied with compressed air was controlled with a simple electrical relay. Albumin was fed into the line prior to a fireball, and when the the fireball event was triggered the solenoid would be opened, forcing out the albumin. In this way it was possible to control the timing of the albumin injection. Before each experiment, the air would be regulated to a low pressure, approximately 1-3 psi. Test shots of simulant would be imaged using a high speed camera to characterize the inherent delay between triggering of the relay and actual simulant injection from the solenoid valve, which was typically approximately 30 ms depending on the exact compressed air pressure upstream of the valve. As a result, the 10.5 ms laser burst could be precisely timed to interact with the BWA-S at the right time.

To visualize the destruction of the bioagent, experiments were conducted with a custom stereoscope built by Gunduz et al and had previously been used to perform pyrometry in mechanically activated nickel-aluminum as well as thermographic phosphorescence measurements in an HMX-binder composite [36, 37]. A schematic of the stereoscope is shown in Figure 5.1 and was designed to separate input light into two separate wavelength bands using bandpass filters. For these experiments, filters were selected to allow 532 nm laser light through one leg and biaogent fluorescence through the other. Both legs are then imaged onto the intensifier photocathode to provide side by side images of the same view but with different wavelengths of light. Fig 5.2 shows the stereoscope integrated into an experimental configuration. By using this stereoscope it is possible to image different diagnostic signals at the same time. The downside to this method is that signal is effectively cut in half due to the 50/50 beam splitter and bandpass filters, however, with the high intensity laser pulses and image intensifier, this was found to be acceptable.
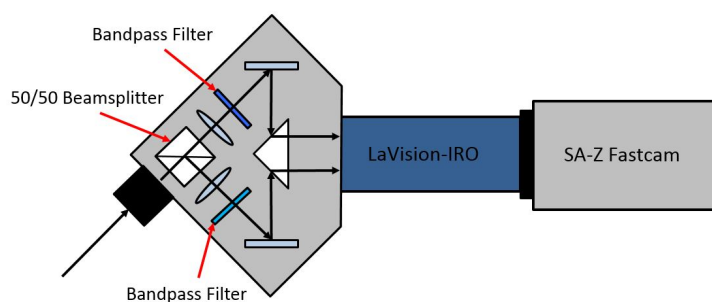
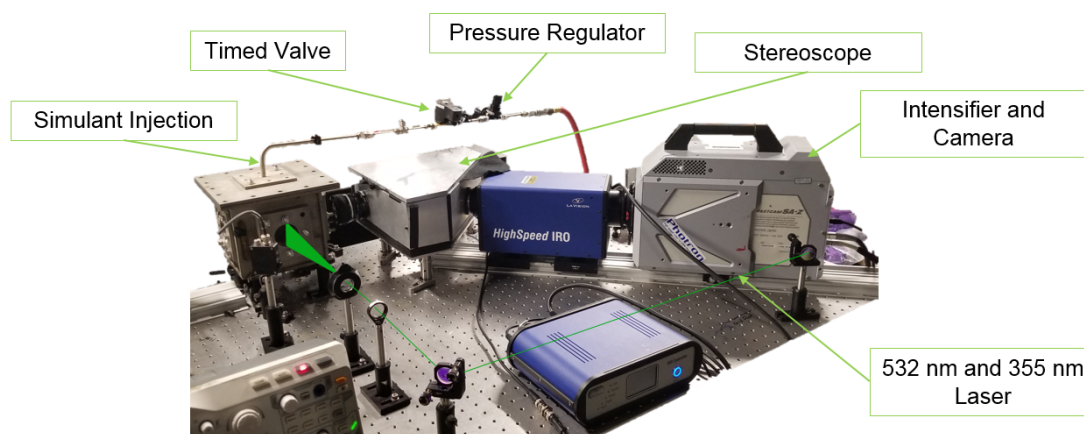Fig. 5.7. The custom stereoscope for imaging different wavelengths.

Fig. 5.8. The experimental setup for bioagent experiments, showing the timed solenoid valve and custom stereoscope.

6. RESULTS AND DISCUSSION

6.1 I_2 PLIF in Fireballs

Figure 6.1 shows the results from PLIF in HMX fireballs. The charges consisted of 100 mg of HMX intimately mixed with 100 mg of I_2. This formulation is likely unrealistic, however an excess of I_2 was used to ensure the collection of high PLIF signals and thus demonstrate the technique. Each image is from a different charge, as each high powered laser burst only allowed for the collection of 10.5 ms of data for each fireball. The laser energy per pulse is approximately 180 mJ, and images were taken with an f-number of 1.2, a gain of 750 volts out of a possible 900, and at a rate of 20 kHz. The field of view for each image is 2 inches by 2 inches. The exposure for each set was 600 ns, except in the case of the 51.5 and 76.5 ms data sets, where a gate of 400 ns was used, and at 26.5 ms, where a gate of 300 ns was used. This was done to reduce the intense flame emission that was reaching the intensifier. This is one of the major issues discovered with conducting I_2 PLIF in combustion reactions, as the emission lifetime is on the order of μ s. As I_2 signal decreases, a longer exposure is desired to capture more fluorescence, but this will also collect more flame emission. As I_2 fluoresces in yellow to red wavelengths, shown in Figure 5.3, color filtering alone is not necessarily sufficient to eliminate flame emission. The filters used were a 532 nm notch filter with an OD of 6, to eliminate laser light, and an OD 6 bandpass filter centered at 592 nm with a full-width half-max of 43 nm. It is possible that the purchase of a custom bandpass filter with a much shorter width and a center wavelength at a shorter fluorescence peak of I_2 could partially alleviate these issues.

Interestingly, there seems to be high signals at the very onset of the fireball, as can be seen in the images at 7.15 ms and 26.5 ms. This suggests that although the fireball is likely quite hot at this time, there is still enough diatomic I_2 produced such

that not all of the I_2 is being dissociated to atomic I by heat. In the context of BWA defeat, this means that a bioagent at the location of the fireball, will likely see a high concentration of both thermal energy and gaseous I_2. Also, clear signal can be seen as late as 5 s after the fireball has occurred. This I_2 persistence and eventual diffusion into the environment will also serve to destroy bioagents. In separate tests not shown, a broadband light source was used to view the I_2 absorption spectra after a fireball, and absorption lines were seen as late as 15 s after the fireball initiation. An example of the laser sheet being blocked by large particles in the fireball is seen in the image at 126.5 ms, another issue encountered in fireball diagnostics.

These images represent qualitative and unprocessed images. The dark spot in the center of the image is due to the image intensifier, which had damage in the center of the photocathode or multichannel plate. In order to correct this, an experiment was conducted to correct each individual pixel. The method for this correction was detailed by Williams and Shaddix and is used for characterizing both the uniformity of the intensifier gain and the intensifier responsivity [38]. In short, a white light source passed through a diffuser and onto a piece of white paper was imaged with the intensifier. Different neutral density (ND) filters with optical densities from 0.1 to 1.0 were then placed in front of the intensifier. It was assumed that the diffuse light source was uniform in spatial intensity. By setting the intensifier to an equal gain setting as used in each experiment, the response of each individual pixel could be characterized for response. An exponential fit operation was carried out for each pixel, with pixel counts being the variable. After constructing a matrix containing this exponential fit for each pixel, PLIF images could be corrected. Figure 6.3 shows the OD and count information for various pixels. The damage can be seen as a reduced signal level at an OD of zero, however the responsivity of the pixels, though damaged, still followed exponential curves. When given a raw PLIF image, a corresponding OD for each pixel is calculated from the raw pixel count. The pixel was then corrected to eliminate this OD. The same images as in Figure 6.1 are shown after this correction

7.15 ms   26.5 ms   51.5 ms

76.5 ms   126.5 ms   251.5 ms

501.5 ms   1.0015 s   5.0015 s
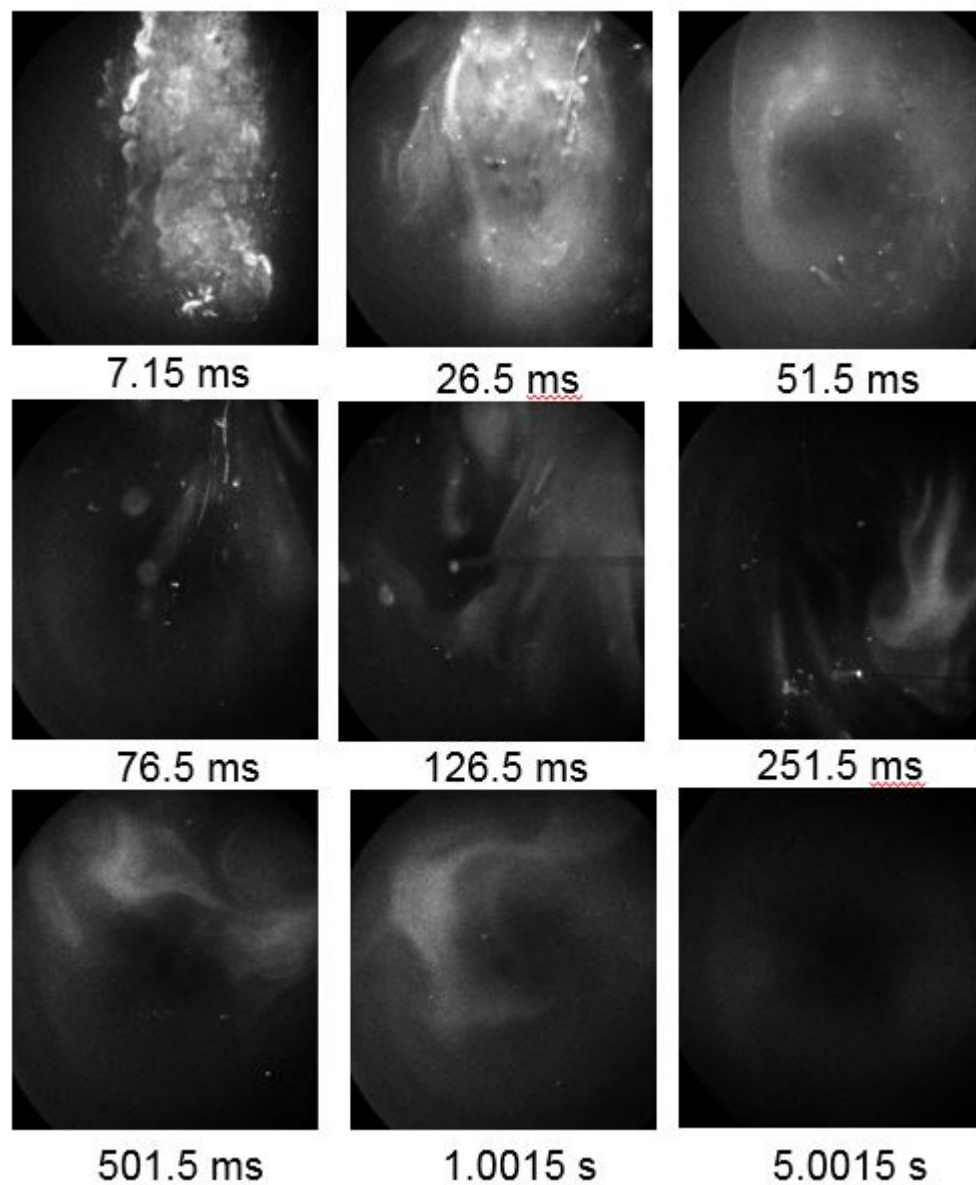
Fig. 6.1. Raw PLIF images taken at rate of 20 kHZ in HMX fireballs.
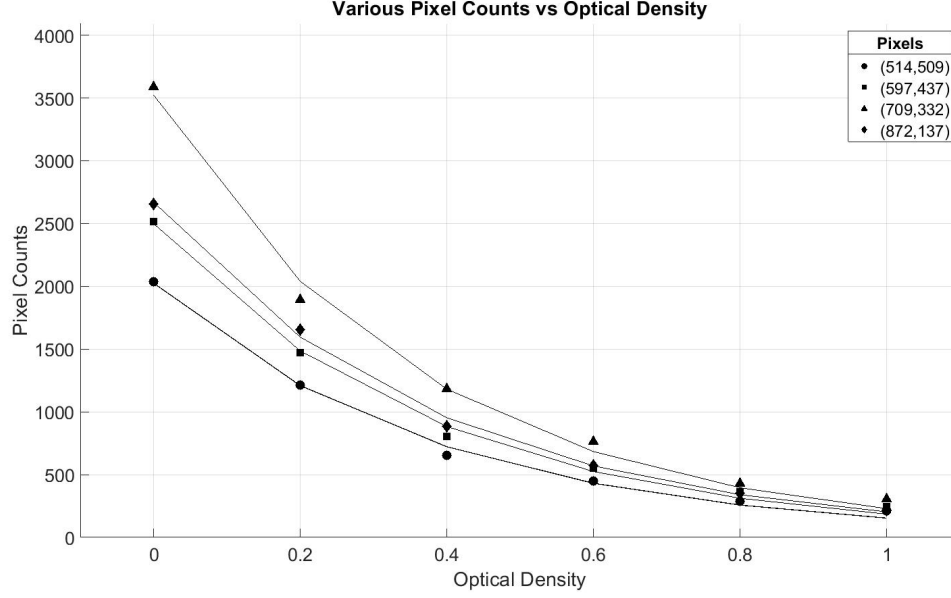
Fig. 6.2. Pixel counts plotted against optical density for various pixels in the intensifier/CMOS system.

procedure in Figure 6.3. A sequence of images from the same laser burst is shown in Figure 6.4. The equation for calculating the corresponding OD was

$$OD_{pixel} = ae^{-bx}. \tag{6.1}$$

A and b are constants from the exponential response function fit to each pixel. The pixel count was then corrected using the equation

$$Counts_{pixel} = (10^{OD_{pixel}})^{-1}. \tag{6.2}$$

This equation gave the pixel count as a decimal from 0 to 1. This value was multiplied by 4095 to match the 12 bit depth of the camera.

The damaged response of the intensifier is largely corrected. This technique is not only useful for correcting damage in equipment, but is also necessary in characterizing the response of the system if quantitative signals are desired. The downside to this technique is the time required to create a data set the corrects the intensifier response

Fig. 6.3. Corrected PLIF images taken at 20 kHz in HMX fireballs.

5 ms   7.5 ms   10 ms

Fig. 6.4. I$_2$ PLIF images taken in the same fireball, showing the evolution of I$_2$ within the early times of an HMX fireball.

and uniformity for each gain setting used experimentally, since the image intensifier response is not necessarily linear to applied gain across the multichannel 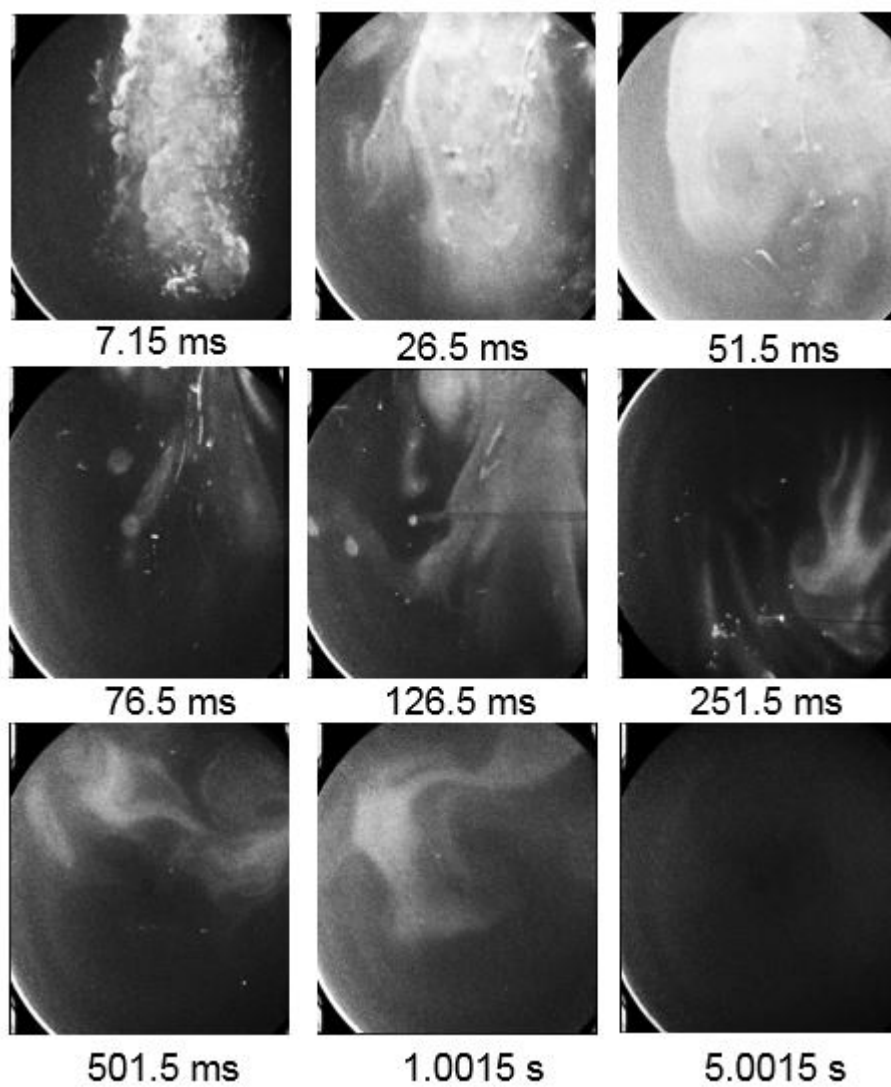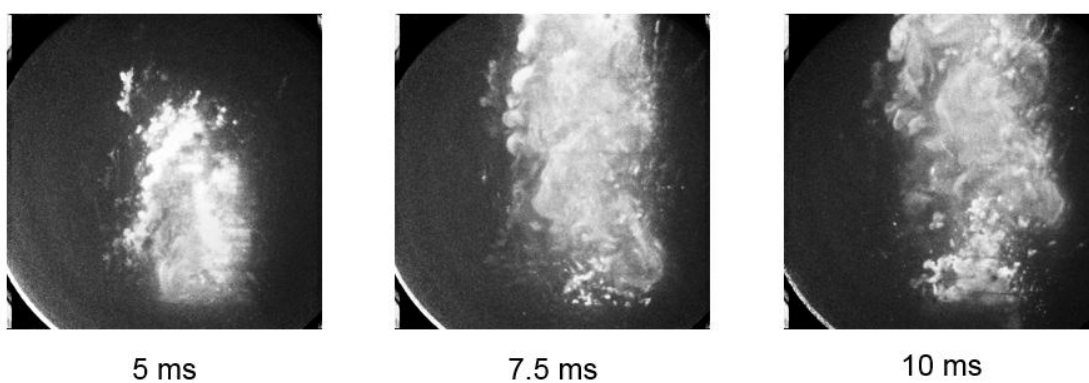plate. Also, to apply the calculated corrections, absolute confidence must be had in the consistency of the coupling between the intensifier and camera. Otherwise, the output light from the intensifier may not be received by the same pixel on the camera from experiment to experiment. In general, collecting the data to perform this correction should be conducted for every experiment, at each gain setting used.

6.2 I_2 Calibrations

Using the constructed calibration cell, multiple tests were conducted in an attempt to improve the LIF diagnostic technique. The most successful tests included wavelength tuning of the Nd:YAG laser cell and will be discussed here as an example of a calibration procedure to improve the PLIF signal. Continuing calibrations will continue to be developed and applied towards a quantitative I_2 measurement.

6.2.1   Nd:YAG Wavelength Tuning

It is possible to slightly alter the lasing wavelength of the pulse-burst Nd:YAG laser by changing the temperature at which the seed laser is kept. However, this not only alters the lasing wavelength but also the power of the laser. Figure 6.5 shows the output power of the pulse-burst Nd:YAG laser as a function of input seed temperature. When tuning to a potential I_2 transition, the power of the laser must be taken into account.

To test the viability of tuning the laser wavelength, the seed temperature was set to 23.87 °C, which accesses the R134(36,0) and P83(33,0) transition at 18787.8 cm^{-1}, about 532.26 nm, in the $X^1\Sigma_g^+$ - $B^3\Pi_{0+u}$ system [39]. The power at this seed temperature is 90% of the maximum power. This was compared to signal found at a temperature of 23.37 °C, which should correspond roughly to the maximum output power of the laser. Figure 6.6 shows example fluorescence images from the constructed
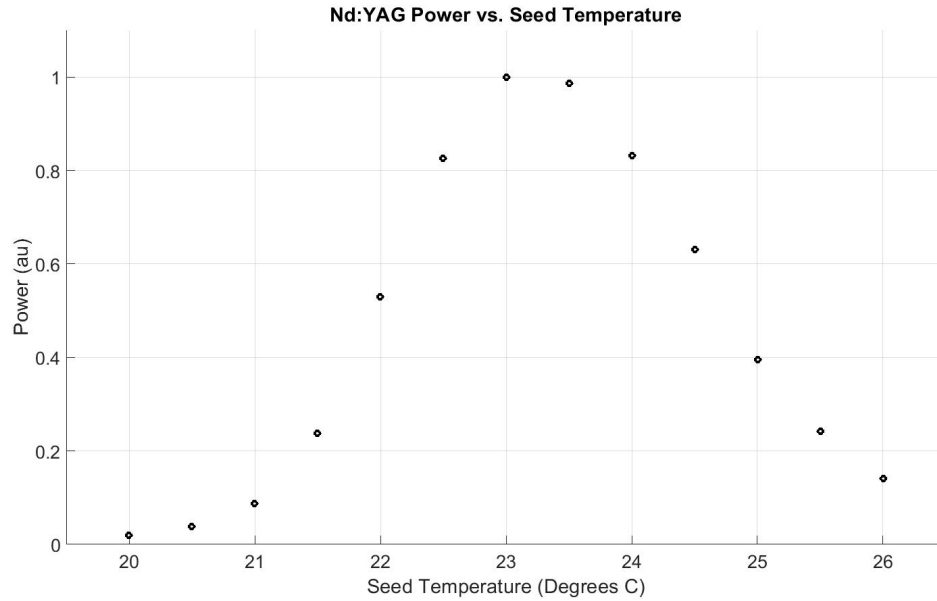
Fig. 6.5. The output power of the Nd:YAG laser with varying input seed temperature normalized to 1.

calibration cell, and Figure 6.7 shows a plot of the integrated fluorescence signal from the two different seed laser temperatures. All tests were conducted at 20 kHz and at a calibration cell temperature of 53.3 °C. The laser energy for the 23.37 °C burst is actually 115.7 % that of the 23.87 °C burst, which serves to further illustrate the improvement in signal that wavelength tuning can result in. At the increased signal levels the intensifier and camera system showed higher shot to shot noise, however the average fluorescence signal was indeed higher.

As demonstrated, tuning of the Nd:YAG laser can greatly increase fluorescence signal even if the energy of the 532 nm laser burst is slightly lower. This is dependent on multiple factors, such as Boltzmann fraction. In the future, temperature diagnostics designed to measure the temperature of a fireball environment, such as imaging pyrometry, will be used to estimate the temperatures that the I_2 gas will be. This can be used to calculate Boltzmann fractions of the I_2 energy levels, such that the wavelength can be further tuned to hit maximum absorption transitions in I_2 gas at

23.37 °C   23.87 °C
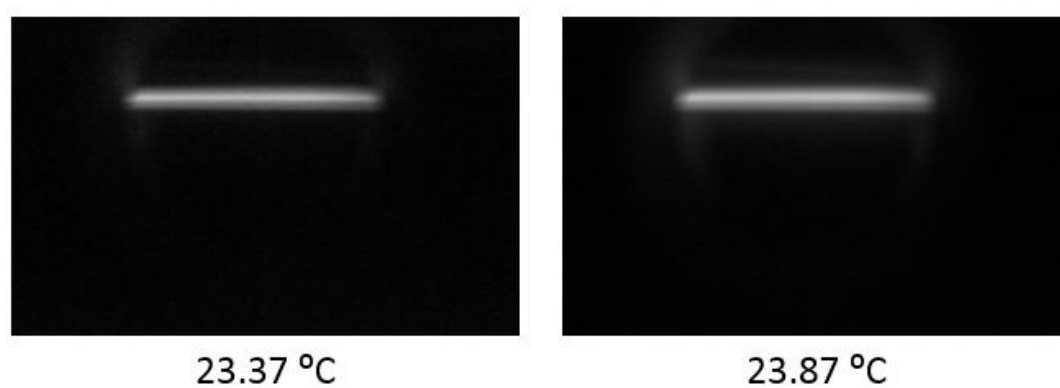
Fig. 6.6. Example fluorescence images acquired in the I_2 calibration cell. Both images were taken at the same time in the burst.
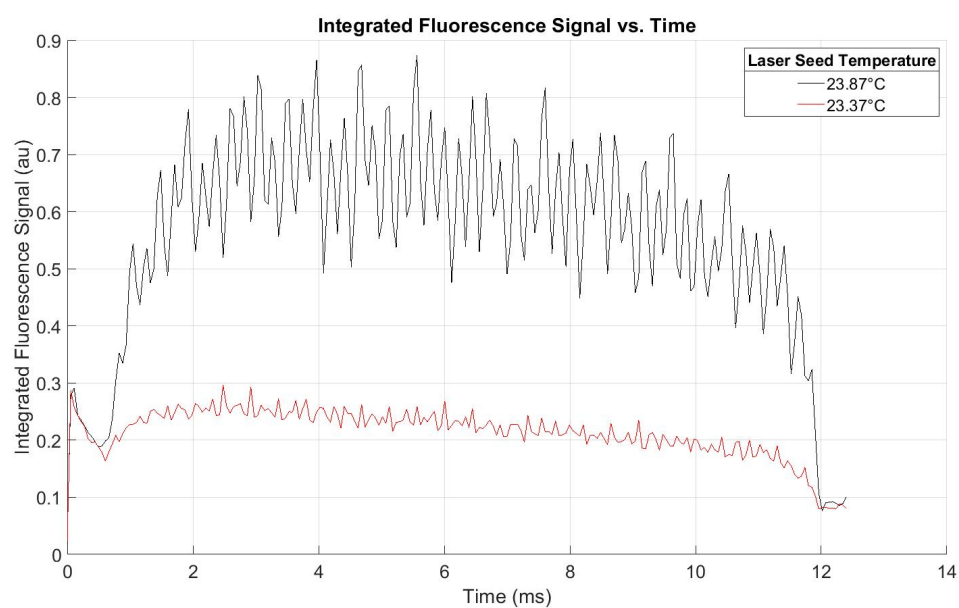
Fig. 6.7. Spatially integrated fluorescence over a laser burst at two different laser seed wavelengths.
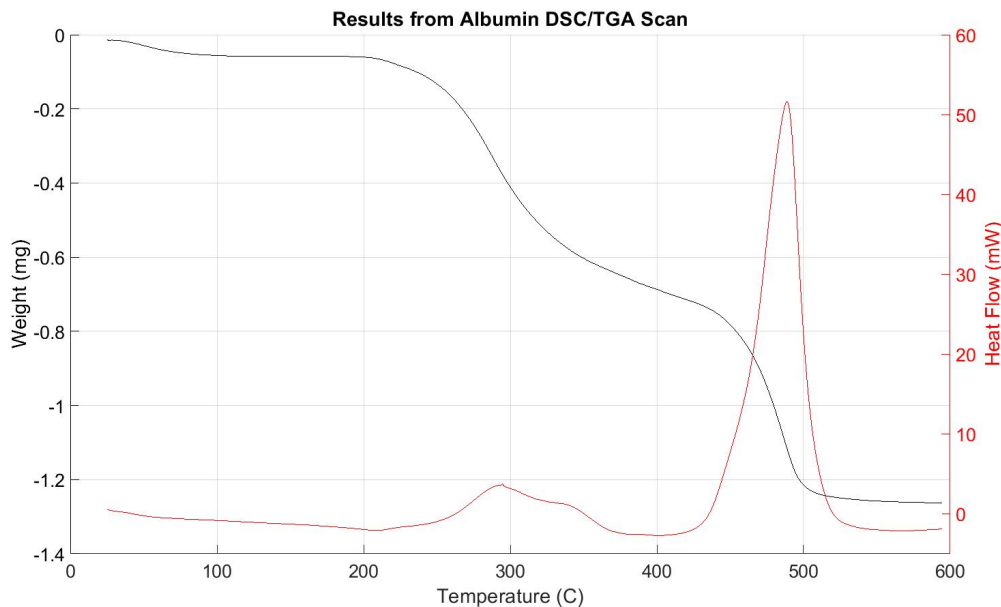
Fig. 6.8. Results from an albumin DSC/TGA scan, showing multiple decomposition steps.

elevated fireball temperatures. In the HMX fireballs shown in Section 6.1, a seed temperature of 23.37 °C was used to provide for maximum laser penetration into the fireball, however, wavelength tuning will be applied in the future to maximize I_2 PLIF signal.

6.3   Bioagents

To first have some idea of the heat destruction of albumin, tests were conducted in a TA Instruments DSC/TGA. The furnace was set to a temperature ramp rate of 10 deg C/min starting at 25 deg C. A 13 mg sample of albumin was placed into an alumina pan in the DSC/TGA and the temperature ramp was started. Two distinct decomposition steps were seen in the resulting data, with one beginning at approximately 200 deg C and another beginning at approximately 400 deg C.

Given that the general decomposition behavior of albumin was now known, another experiment was conducted to determine if any decrease in fluorescence signal
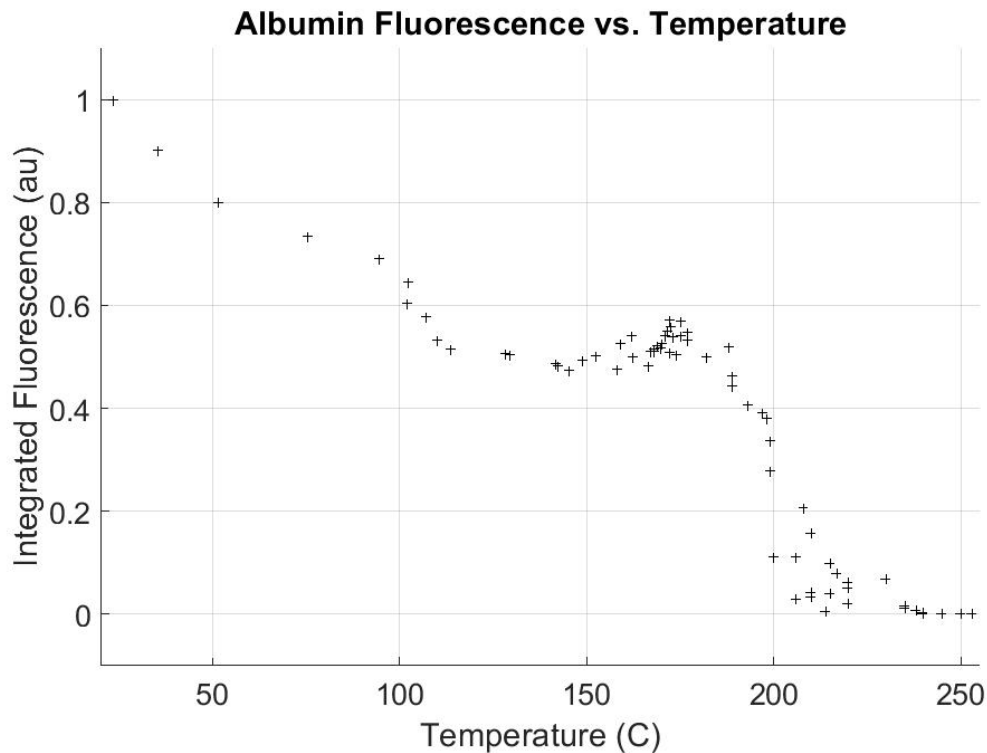
Fig. 6.9. Integrated albumin fluorescence during heating on a hot plate.

could be seen as albumin was heated. For this experiment, albumin was placed onto a hot plate, and 355 nm laser light was aligned to the albumin. A 100 mm spherical lens was placed such that emitted fluorescence was imaged onto a spectrometer slit and spectra were recorded every 10 seconds, which was the burst repetition rate of the laser. The laser was pulsed at 20 kHz to maximize the amount of fluorescence signal received by EMCCD camera imaging the spectrometer. A infrared thermometer was used to read the surface temperature of the albumin powder. Figure 6.9 shows the fluorescence intensity imaged from 380 to 525 nm against temperature.

Interestingly, the fluorescence heating test showed a similar two step curve as the DSC/TGA analysis, however at lower temperatures. It is possible that this is due to the different heating rates. In the DSC/TGA, a slow ramp of 10 deg C/min was used, while each data point in the hot plate test represents 10 seconds. However, these tests made it clear that given exposure to high temperatures, albumin will experience both

mass loss and loss of fluorescence emission. As exposure to high fireball temperatures will be on timescales of hundreds of milliseconds or less, the heat absorbed must be similar to the DSC/TGA and hot plate tests to see a decrease in fluorescence.

Since it was proven that exposure of albumin to high heats could result in a lack of fluorescence signal, tests were conducted within fireballs to see if a decrease in fluorescence signal could be seen. In initial tests, it appeared that simulant fluorescence was being reduced by exposure to fireballs. To prove that the loss of fluorescence was due to BWA-S destruction, the custom stereoscope was used to image both laser scattering at 532 nm and the bioagent simulant fluorescence produced by 355 nm excitation. The simulant fluorescence signal was isolated by a 447 nm bandpass filter and the 532 nm scattering signal was isolated by a 528 nm bandpass filter. Both of these probe wavelengths were generated from the same pulse-burst Nd:YAG laser and made to propagate across the same path. Figure 6.8 shows a series of images of bioagent simulants injected into a fireball produced by 100 mg of HMX at different time delays. Fluorescence signal is negligible until 104 ms, when the peak temperature of the fireball has passed. This suggested that the fireball was effectively neutralizing the bioagent simulants via heat. Fireball luminosity was effectively reduced by both short camera exposures and bandpass filters. In the final frame at 128 ms, it can be seen that the fluorescence and scattering signals are comparable. Given that scattering particles were seen in the earlier fireball times, it was theorized that the BWA-S was experiencing sufficient heat transfer to cause a lack of fluorescence.

However, it was not certain that the lack of fluorescence signal seen in fireballs test was due to BWA-S destruction or by another cause such as fireball optical depth. Fireball optical depth could both limit the 355 nm light reaching the BWA-S, and the BWA-S fluorescence emission escaping the fireball. Figure 6.9 shows an example image of a bioagent simulant imaged through the stereoscope in the absence of a fireball, as well as a thermographic phosphor, BaMgAl10O17:Eu2+ (BAM) in a fireball. BAM is capable of withstanding high temperatures and phosphoresces strongly following 355 nm excitation, and was chosen as an inert tracer to determine if the 355
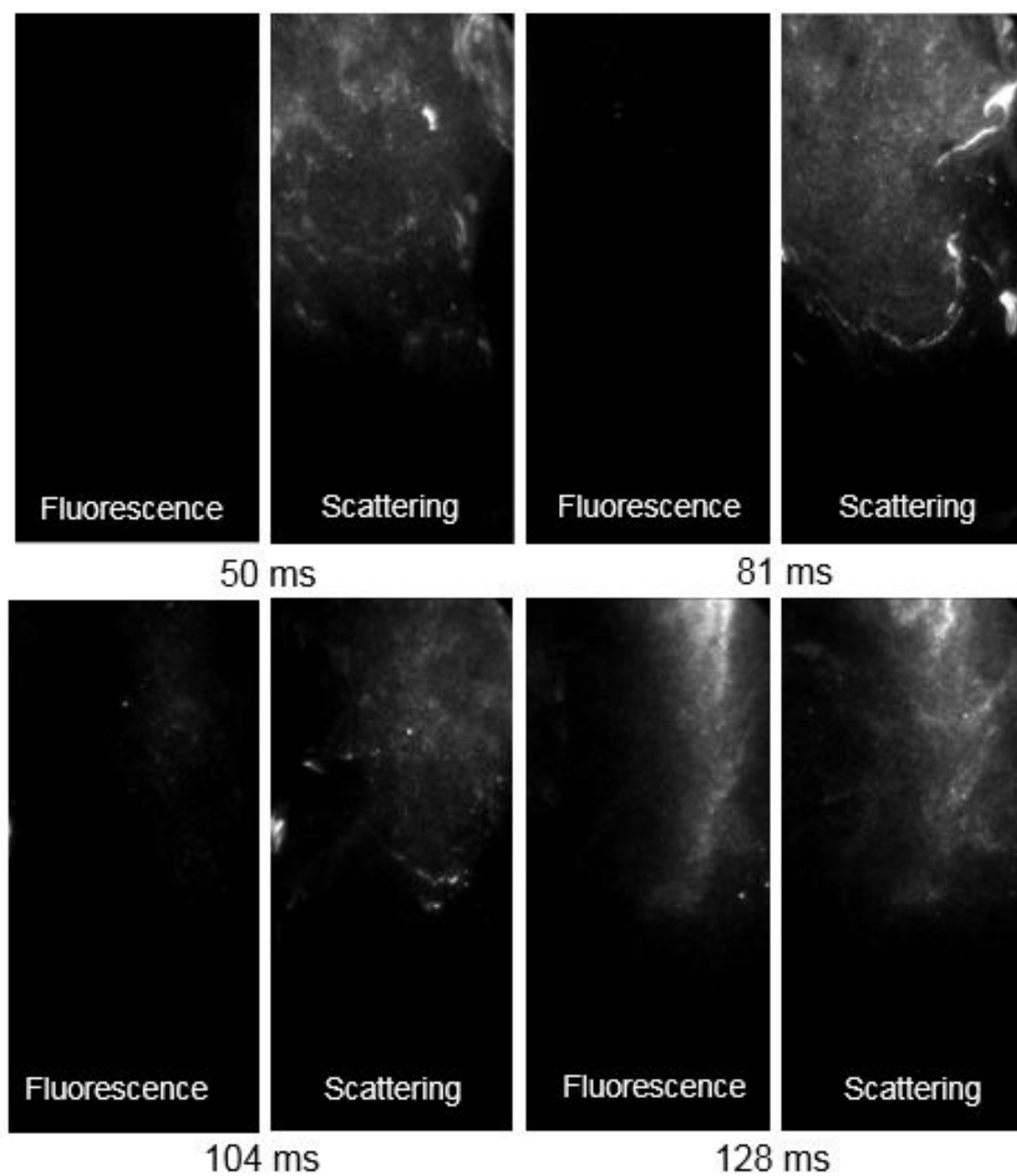
Fig. 6.10. Bioagent fluorescence and scattering imaged in the stereoscope at different injection times in a fireball event.
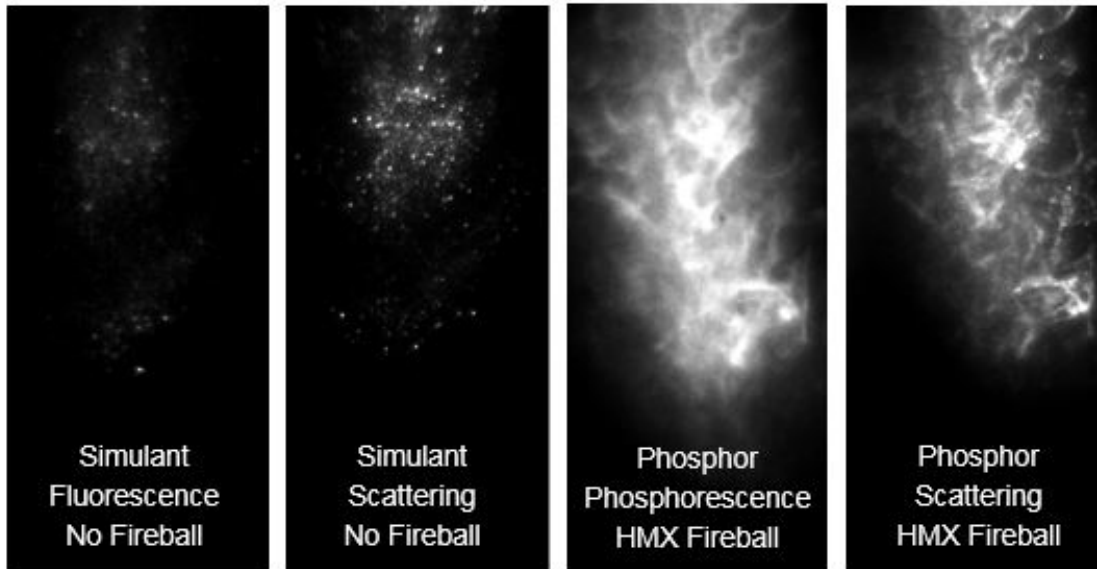
Fig. 6.11. Simulant fluorescence and scattering imaged without a fireball event compared to phosphor phosphorescence and scattering imaged in a fireball.

nm laser power was sufficient to excite particles within the fireball. Neutral density filters were inserted into the stereoscope to make both the scattering and fluorescence images on the camera approximately equal in signal level.

From the phosphorescence images taken in fireballs, it was clear that the laser light was penetrating the fireball and exciting possible material inside the fireball. As the phosphorescence signal was not appreciably decreased, this experiment increased confidence in the ability of the stereoscope diagnostic to image BWA-S destruction within a fireball. The scattering measurements can provide insight into both particle location and fireball evolution, while fluorescence may be used to measure BWA-S defeat.

6.4 I_2 Modeling

Significant effort was also devoted to the development of an absorption and fluorescence model for I_2 in order to better understand the photophysics associated with

conducting I_2 PLIF in reaction. A discussion of methods and results for this modeling will be discussed here.

The basis for the model lies within the use of Boltzmann calculations to determine populations in various energy levels at the elevated temperatures seen in combustion reactions. A detailed discussion of Boltzmann calculations is included in Appendix B. The location of absorption lines are calculated using the electronic, vibrational, and rotational energies of every possible transition. In this way, each individual absorption line could be calculated and summed together in order to reconstruct the entire visible absorption spectrum.

The method used to calculate the frequency of individual transitions was based on the equations and constants provided by Gerkstenkom and Luc [40]. The equation for calculating the frequency of the v' level is

$$E(v', J) = E_{v'}(0) + B_{v'}K - D_{v'}K^2 + H_{v'}K^3 + L_{v'}K^4 + M_{v'}K^5. \quad (6.3)$$

The equation for calculating the frequency of the v" level is

$$E(v", J) = E_{v"}(0) + B_{v"}K - D_{v"}K^2 + H_{v"}K^3. \quad (6.4)$$

K is equal to J(J+1), and all other constants are given by Gerkstenkom and Luc, and are dependent on the vibrational and rotational level [40]. The frequency of transition is then the difference between Equations 6.3 and 6.4. To model the absorption curve, all vibrational and rotational levels from v"=0 to v"=10 and J"=0 to J"=200 and v'=0 to v'=50 are calculated. After this, the relevant Boltzmann fraction and Franck-Condon factor is applied to the transition such that the relative strength of the transition is calculated for the prescribed temperatures.

The lineshapes of the absorption lines are calculated using a Voigt fitting method described by McLean, and is dependent on collisional and Doppler broadening effects [41]. Collisional broadening is dependent on populations of ambient and I_2 molecules, as well as temperature. From the strength of transition and lineshape, the absorption
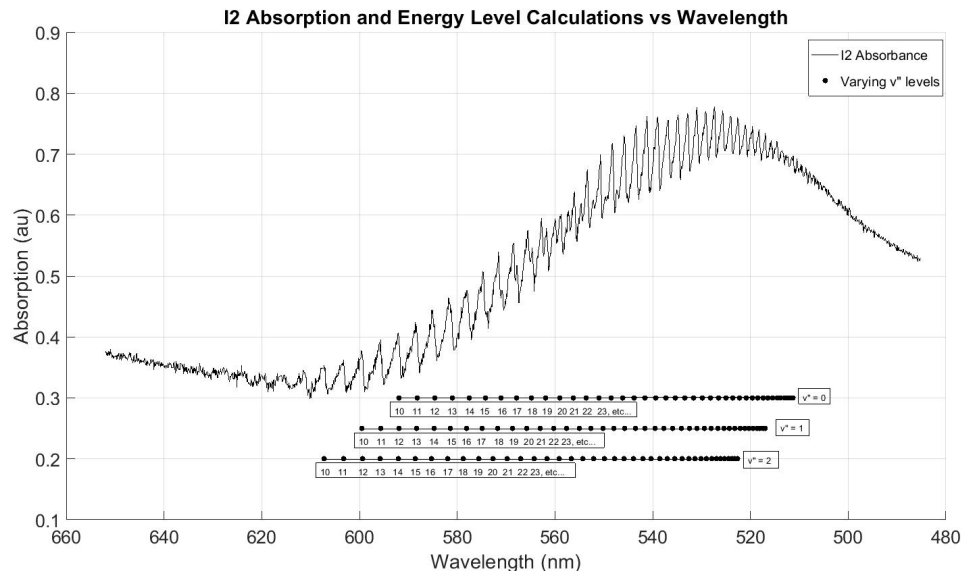
Fig. 6.12. Simulated I_2 absorption at 300K and 2 kPa I_2.

transitions are known can be summed to create the visible I_2 absorption spectrum. Figure 6.12 shows the calculated I_2 absorption spectrum at 300 K. Line positions match that found in literature. Figure 6.13 shows a preliminary fluorescence model at 300 K based on Franck-Condon factors found in literature. Intensities vary from those found experimentally in Figure 5.3, which calls into question the Franck-Condon factors used. Further development of the fluorescence model is ongoing and will be compared against experimental data to validate the model. Once sufficient confidence is reached in the accuracy of the fluorescence model, experimental parameters such as collisional quenching will be applied to the model to predict signal levels.
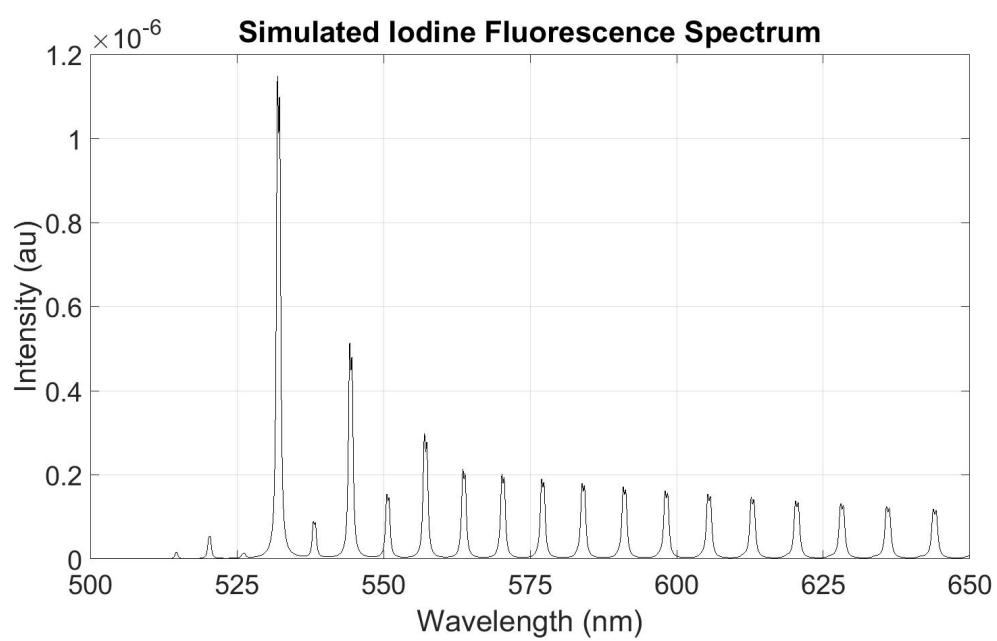
Fig. 6.13. Simualted I$_2$ fluorescence model at 300 K.

7. SUMMARY

High-speed planar laser induced fluorescence has been successfully applied in fireballs to both the biocidal species I_2 and the BWA-S albumin. The diagnostic approach provides the capability to spatio-temporally resolve the interaction of species within reacting fireballs by utilizing a high-powered Nd:YAG pulse-burst laser and high-speed intensified cameras. Preliminary calibration studies were performed on I_2 to give insight into improving the PLIF measurement and moving towards a quantitative species concentration measurement. In the future, further calibration experiments can be conducted to allow estimates of the species concentrations from the fluorescence signals.

I_2 is produced early in the reaction, largely following the fireball evolution. However, I_2 is seen to persist for seconds after the fireball has concluded, where the intense heat from the fireball has subsided and will not likely continue to kill BWAs. However, I_2 can bolster the biocidal effectiveness of a munition, and the PLIF diagnostic technique is demonstrated to be promising for determining the behavior of I_2 produced by a fireball. By conducting further studies of concentration after a fireball has subsided, conclusions into the potential of different I_2 containing munitions may be evaluated for biocidal effectiveness.

A technique to image BWA destruction has been devised and applied to albumin. Scattering and fluorescence tests were performed simultaneously to view if any loss of fluorescence signal relative to the scattering signal could be imaged. The technique was also applied to a ceramic phosphorescent material to verify that the laser energy was sufficient to penetrate the fireball. Differences between the temperature resistant material and the BWA-S can then be used to identify thermo-chemically induced changes in the BWA-S in different fireball environments.

A model for I_2 absorption was developed to give insight into conducting PLIF experiments at various conditions. The model accurately predicts the I_2 absorption spectrum and lays the foundation for a fluorescence spectroscopy model that can be used for interpreting I_2 fluorescence signals. Future work includes further development of this model, including effects of quenching at various flame conditions.

These tests provide a method of studying fireballs for BWA defeat purposes. To the author's knowledge, these results provide the first demonstration of I_2 PLIF performed in combustion reactions. Moving forward, future work is needed improve the calibrations and advance the I_2 PLIF measurements in order to move towards quantitative species concentration measurements in agent defeat fireballs.

REFERENCES

REFERENCES

[1] E. M. Eitzen and E. T. Takafuji, "Historical overview of biological warfare," *Medical aspects of chemical and biological warfare*, pp. 415–423, 1997.

[2] H.-J. Jansen, F. J. Breeveld, C. Stijnis, and M. P. Grobusch, "Biological warfare, bioterrorism, and biocrime," *Clinical Microbiology and Infection*, vol. 20, no. 6, pp. 488–496, 2014.

[3] T. V. Inglesby, D. A. Henderson, J. G. Bartlett, M. S. Ascher, E. Eitzen, A. M. Friedlander, J. Hauer, J. McDade, M. T. Osterholm, T. O'Toole *et al.*, "Anthrax as a biological weapon: medical and public health management," *Jama*, vol. 281, no. 18, pp. 1735–1745, 1999.

[4] L. J. Rose and H. O'Connell, "Uv light inactivation of bacterial biothreat agents," *Applied and Environmental Microbiology*, vol. 75, no. 9, pp. 2987–2990, 2009. [Online]. Available: https://aem.asm.org/content/75/9/2987

[5] M. May and Z. Haldeman, "Effectiveness of nuclear weapons against buried biological agents," *Science and Global Security*, vol. 12, no. 1-2, pp. 91–113, 2004.

[6] W. L. Nicholson, N. Munakata, G. Horneck, H. J. Melosh, and P. Setlow, "Resistance of bacillus endospores to extreme terrestrial and extraterrestrial environments," *Microbiol. Mol. Biol. Rev.*, vol. 64, no. 3, pp. 548–572, 2000.

[7] A. Russell, "Bacterial spores and chemical sporicidal agents." *Clinical microbiology reviews*, vol. 3, no. 2, pp. 99–119, 1990.

[8] T. Kaiho, *Iodine chemistry and applications.* Wiley Online Library, 2014.

[9] H. Wang, G. Jian, W. Zhou, J. DeLisio, V. Lee, and M. Zachariah, "Metal iodate-based energetic composites and their combustion and biocidal performance," *ACS applied materials & interfaces*, vol. 7, no. 31, pp. 17 363–17 370, 2015.

[10] S. Zhang, M. Schoenitz, and E. L. Dreizin, "Iodine release, oxidation, and ignition of mechanically alloyed al- i composites," *The Journal of Physical Chemistry C*, vol. 114, no. 46, pp. 19 653–19 659, 2010.

[11] S. Zhang, C. Badiola, M. Schoenitz, and E. L. Dreizin, "Oxidation, ignition, and combustion of al· i2 composite powders," *Combustion and Flame*, vol. 159, no. 5, pp. 1980–1986, 2012.

[12] A. Abraham, J. Obamedo, M. Schoenitz, and E. L. Dreizin, "Effect of composition on properties of reactive al· b· i2 powders prepared by mechanical milling," *Journal of Physics and Chemistry of Solids*, vol. 83, pp. 1–7, 2015.

[13] S. Wang, M. Schoenitz, and E. L. Dreizin, "Mechanically alloyed magnesium–boron–iodine composite powders," *Journal of Materials Science*, vol. 51, no. 7, pp. 3585–3591, 2016.

[14] C. E. Johnson and K. T. Higa, "Iodine-rich biocidal reactive materials," *MRS Online Proceedings Library Archive*, vol. 1521, 2013.

[15] J. Feng, G. Jian, Q. Liu, and M. R. Zachariah, "Passivated iodine pentoxide oxidizer for potential biocidal nanoenergetic applications," *ACS applied materials & interfaces*, vol. 5, no. 18, pp. 8875–8880, 2013.

[16] S. Wang, X. Liu, M. Schoenitz, and E. L. Dreizin, "Nanocomposite thermites with calcium iodate oxidizer," *Propellants, Explosives, Pyrotechnics*, vol. 42, no. 3, pp. 284–292, 2017.

[17] B. R. Clark and M. L. Pantoya, "The aluminium and iodine pentoxide reaction for the destruction of spore forming bacteria," *Physical Chemistry Chemical Physics*, vol. 12, no. 39, pp. 12 653–12 657, 2010.

[18] S. A. Grinshpun, A. Adhikari, M. Yermakov, T. Reponen, E. Dreizin, M. Schoenitz, V. Hoffmann, and S. Zhang, "Inactivation of aerosolized bacillus atrophaeus (bg) endospores and ms2 viruses by combustion of reactive materials," *Environmental science & technology*, vol. 46, no. 13, pp. 7334–7341, 2012.

[19] Y. Aly, S. Zhang, M. Schoenitz, V. Hoffmann, E. Dreizin, M. Yermakov, R. Indugula, and S. Grinshpun, "Iodine-containing aluminum-based fuels for inactivation of bioaerosols," *Combustion and Flame*, vol. 161, no. 1, pp. 303–310, 2014.

[20] O. Cenciarelli, S. Pietropaoli, V. Gabbarini, M. Carestia, F. D'Amico, A. Malizia, M. Gelfusa, R. Pizzoferrato, A. Sassolini, D. Di Giovanni *et al.*, "Use of non-pathogenic biological agents as biological warfare simulants for the development of a stand-off detection system," *J. Microb. Biochem. Technol*, vol. 6, pp. 375–380, 2014.

[21] Y.-L. Pan, J. D. Eversole, P. H. Kaye, V. Foot, R. G. Pinnick, S. C. Hill, M. W. Mayo, J. R. Bottiger, A. Huston, V. Sivaprakasam *et al.*, "Bio-aerosol fluorescence," in *Optics of biological particles.* Springer, 2007, pp. 63–164.

[22] M. Kaliszewski, M. Włodarski, J. Młyńczak, M. Leśkiewicz, A. Bombalska, M. Mularczyk-Oliwa, M. Kwaśny, D. Buliński, and K. Kopczyński, "A new real-time bio-aerosol fluorescence detector based on semiconductor cw excitation uv laser," *Journal of Aerosol Science*, vol. 100, pp. 14–25, 2016.

[23] Ø. Farsund, G. Rustad, and G. Skogan, "Standoff detection of biological agents using laser induced fluorescence—a comparison of 294 nm and 355 nm excitation wavelengths," *Biomedical optics express*, vol. 3, no. 11, pp. 2964–2975, 2012.

[24] R. Lodes, H. Krier, and N. Glumac, "Spectrally-and-temporally-resolved optical depth measurements in high explosive post-detonation fireballs," *Propellants, Explosives, Pyrotechnics*, vol. n/a, no. n/a. [Online]. Available: https://onlinelibrary.wiley.com/doi/abs/10.1002/prep.201900225

[25] B. Hiller and R. Hanson, "Properties of the iodine molecule relevant to laser-induced fluorescence experiments in gas flows," *Experiments in fluids*, vol. 10, no. 1, pp. 1–11, 1990.

[26] J. Lehmann, "Iodine, a test molecule in modern spectroscopy," *Contemporary Physics*, vol. 19, no. 5, pp. 449–467, 1978.

[27] K. Sakurai, G. Capelle, and H. Broida, "Measurements of lifetimes and quenching cross sections of the b 3 π 0u+ state of iodine using a tunable dye laser," *The Journal of Chemical Physics*, vol. 54, no. 3, pp. 1220–1223, 1971.

[28] T. Masiello, N. Vulpanovici, and J. W. Nibler, "Fluorescence lifetime and quenching of iodine vapor," *Journal of chemical education*, vol. 80, no. 8, p. 914, 2003.

[29] J. Simmons and J. Hougen, "Atlas of the l2 spectrum from 19 000 to 18 000 cm-i," *TC*, vol. 6, no. 6, p. 6, 1977.

[30] J. C. Lehmann, "Laser spectroscopy and predissociation of molecules," pp. 167–178, 1977.

[31] L. Brewer and J. Tellinghuisen, "Quantum yield for unimolecular dissociation of i2 in visible absorption," *The Journal of Chemical Physics*, vol. 56, no. 8, pp. 3929–3938, 1972.

[32] R. K. Hanson, R. M. Spearrin, and C. S. Goldenstein, *Spectroscopy and optical diagnostics for gases.* Springer, 2016.

[33] R. R. Bernecker and L. C. Smith, "On the products formed in the combustion of explosives. freeze-out in the water-gas reaction," *The Journal of Physical Chemistry*, vol. 71, no. 8, pp. 2381–2390, 1967.

[34] M. N. Slipchenko, J. D. Miller, S. Roy, J. R. Gord, S. A. Danczyk, and T. R. Meyer, "Quasi-continuous burst-mode laser for high-speed planar imaging," *Optics Letters*, vol. 37, no. 8, pp. 1346–1348, 2012.

[35] J. M. Peuker, P. Lynch, H. Krier, and N. Glumac, "Optical depth measurements of fireballs from aluminized high explosives," *Optics and Lasers in Engineering*, vol. 47, no. 9, pp. 1009–1015, 2009.

[36] A. Justice, I. E. Gunduz, and S. F. Son, "Microscopic two-color infrared imaging of nial reactive particles and pellets," *Thin Solid Films*, vol. 620, pp. 48–53, 2016.

[37] A. D. Casey, Z. A. Roberts, A. Satija, R. P. Lucht, T. R. Meyer, and S. F. Son, "Dynamic imaging of the temperature field within an energetic composite using phosphor thermography," *Applied Optics*, vol. 58, no. 16, pp. 4320–4325, 2019.

[38] T. C. Williams and C. R. Shaddix, "Simultaneous correction of flat field and nonlinearity response of intensified charge-coupled devices," *Review of Scientific Instruments*, vol. 78, no. 12, p. 123702, 2007.

[39] J. N. Forkey, W. R. Lempert, and R. B. Miles, "Corrected and calibrated i 2 absorption model at frequency-doubled nd: Yag laser wavelengths," *Applied optics*, vol. 36, no. 27, pp. 6729–6738, 1997.

[40] S. Gerstenkom and P. Luc, "Description of the absorption spectrum of iodine recorded by means of fourier transform spectroscopy: the (bx) system," *Journal de Physique*, vol. 46, no. 6, pp. 867–881, 1985.

[41] A. McLean, C. Mitchell, and D. Swanston, "Implementation of an efficient analytical approximation to the voigt function for photoemission lineshape analysis," *Journal of Electron Spectroscopy and Related Phenomena*, vol. 69, no. 2, pp. 125–132, 1994.

[42] N. M. Laurendeau, *Statistical thermodynamics: fundamentals and applications.* Cambridge University Press, 2005.

[43] *NIST Chemistry WebBook, NIST Standard Reference Database Number 69, Eds. P.J. Linstrom and W.G. Mallard.*

APPENDICES

A. POTENTIAL BIOAGENTS

TABLE I. Selected biological agents potentially involved in bioterrorism

Disease	Agent	Organism persistence	Infective dose	Human-to-human transmission	Infectivity	Incubation period	Symptoms	Mortality	Treatment
Anthrax	Spores of Bacillus anthracis	Very stable, spores may be viable for >40 years in soil	8000-50 000 spores	No	–	1-6 days	Fatigue, fever, malaise, cough, mild chest discomfort, respiratory distress, shock	High	Ciprofloxacin or doxycycline
Brucellosis	Genus Brucella (B. melitensis, B. suis, B. abortus, B. canis)	6 weeks. In dust to 10 weeks. In soil or water	10-100 organisms	No	–	5-60 days	Fever, headache, malaise, chills, sweating, myalgia, arthralgia, depression	5% if untreated	Doxycycline + rifampicin
Glanders	Burkholderia mallei	Very stable	Unknown	Rare but possible	–	10-14 days	Pulmonary form: cough, chest pain, fever, rigors, sweating, pleuritis	Very high if untreated	Ceftazidime, imipenem, or meropenem. Post-exposure prophylaxis with co-trimoxazole
Melioidosis	Burkholderia pseudomallei	Very stable	Unknown	Rare but possible	–	10-14 days		Very high if untreated	Streptomycin or gentamicin with ciprofloxacin or doxycycline
Plague	Yersinia pestis	Up to 1 year in soil, but viable only for 1 h after aerosol release	100-20 000 organisms	High	Patients contagious for up to 3 days after starting treatment	1-6 days	High fever, headache, malaise, chest pain, cough, haemoptysis, dyspnoea, stridor, cyanosis	Very high if untreated, <10% with antibiotics	Tetracycline or doxycycline
Q-fever	Coxiella burnetii	Resistant to heat and drying, persists for weeks to months	1-10 organisms	Rare but possible	Up to 4-5 weeks in faeces	7-41 days	Fever, chills, headache, malaise, fatigue, anorexia, weight loss, endocarditis (as presenting symptom of chronic disease)	1% untreated, chronic form 30-60%	Tetracycline or doxycycline
Salmonellosis	Genus Salmonella (S. typhi, S. paratyphi)	Resistant to heat up to 57-60°C	Unknown	Faecal-oral transmission	Up to 4-5 weeks in faeces	6-48 h	Nausea, vomiting, mucopurulent or bloody diarrhoea, abdominal cramps, headache, maculopapular exanthema	<1%	Supportive care to prevent dehydration. In severe infections fluoroquinolones or third-generation cephalosporins
Shigellosis	Genus Shigella (S. dysenteriae, S. flexneri, S. sonnei and S. boydii)	Mean survival of 2-3 days, up to 17 days in favourable circumstances, several hours on infected hands	10-100 organisms	Faecal-oral transmission	In acute phase, high excretion in faeces, without antibiotic treatment, up to 4 weeks	1-7 days	Fever, abdominal cramps, diarrhoea, haemorrhagic colitis	<1%	Usually self-limiting. In severe infections, trimethoprim-sulphamethoxazole and ciprofloxacin shorten duration of symptoms and excretion in faeces
Tularaemia (rabbit fever)	Francisella tularensis ssp. tularensis	Weeks in water, soil, or carcasses, and years in frozen meat	10-50 organisms	No	–	1-25 days (mean 3-5 days)	Fever, chills, myalgia, arthralgia, headache, nausea, vomiting, diarrhoea, sore throat	4-50% mortality without treatment. With treatment, 1%	Streptomycin or gentamicin
Smallpox	Variola virus: Variola major	Highly stable for up to 1 year in dust and cloth	10-100 organisms	Yes, transmission requires close contact	Mostly contagious during first week of rash	4-19 days (mean 10-12 days)	Severe headache, high fever, extreme prostration, backache, chest and join pains, anxiety, exanthema, maculopapular rash that becomes vesicular	Ordinary-type smallpox: 30% if unvaccinated; 3% if vaccinated	No antiviral treatment, vaccination immediately or up to 4 days after exposure can reduce mortality
Venezuelan equine encephalitis	Alphavirus, (Venezuelan equine)	Unstable in environment	10-100 organisms	No	–	2-6 days	Malaise, spiking fevers, rigors, headache, myalgia, nausea,	<1%	Supportive treatment

Fig. A.1. Bioagents with potential for biocrime and or bioterrorism, from Jansen et al [2]

B. BOLTZMANN CALCULATIONS

The Boltzmann distribution can be used to describe the population of atoms or molecules in a certain energy levels. Equations in this appendix are based from Laurendeau's text on statistical thermodynamics [42]. Constants are taken from the NIST Chemistry WebBook [43]. The equation for the fraction of particles in the arbitrary state i is

$$\frac{N_i}{N} = \frac{g_i e^{\frac{-E_i}{k_b T}}}{Z(T)}, \tag{B.1}$$

where N is population, g_i is the degeneracy of the level, k_B is the Boltzmann coefficient, E_i is the energy of the level, T is temperature, and $Z(T)$ is the partition function, which describes how particles are partitioned amongst energy levels, and is defined as

$$Z(T) = \sum_i g_i e^{\frac{-E_i}{k_B T}}. \tag{B.2}$$

For laser induced fluorescence, the Boltzmann distribution of I_2 molecules in different vibrational and rotational levels in the ground electronic state will determine the number of molecules that will be excited by a photon of particular wavelength. The equations for calculating the partition functions and energies of various vibrational and rotational levels are shown below.

B.1 Rotational Distribution

The equation for calculating the energy of a rotational state J is

$$E_j = hcJ(J+1)B_e, \tag{B.3}$$

where h is Planck's constant, c is the speed of light, J is the rotational level, and B_e is the equilibrium rotational constant.

The rotational degeneracy g_J is

$$g_J = 2J + 1. \tag{B.4}$$

Substituting Equations (B.3) and (B.4) into (B.2), the rotational partition function $Z_{rot}(T)$ becomes

$$Z_{rot}(T) = \sum_J (2J+1)e^{\frac{-hcJ(J+1)B_e}{k_B T}}. \tag{B.5}$$

However, the characteristic rotational temperature Θ_r,

$$\Theta_r = \frac{hcB_e}{k_B} \tag{B.6}$$

can be substituted, leading to

$$Z_{rot}(T) = \sum_J (2J+1)e^{\frac{-J(J+1)\Theta_r}{T}}. \tag{B.7}$$

However, this equation overcounts the number of quantum states for a diatomic molecule such as I_2, the root of which lies in the indistinguishability of the atoms in the molecule. A detailed explanation can be found on page 182 of [42], and is beyond the scope of this work. In short, this can be corrected by the introduction of a symmetry factor σ, which is equal to one for heteronuclear diatomics and equal to two for homonuclear diatomics. Equation (B.7) becomes

$$Z_{rot}(T) = \frac{1}{\sigma}\sum_J (2J+1)e^{\frac{-J(J+1)\Theta_r}{T}}. \tag{B.8}$$

For I_2, Θ_r is equal to about 0.0538 K. By using a Euler-Maclaurin expansion, also detailed by Laurendeau, the rotational partition function can be reduced to

$$Z_{rot}(T) = \frac{T}{\sigma\Theta_r}, \tag{B.9}$$

given that $T \gg \Theta_r$. As such, for rotational energy levels, Equation (B.1) becomes

$$\frac{N_J}{N} = \frac{(2J+1)e^{\frac{-hcJ(J+1)B_e}{k_bT}}}{\frac{T}{\sigma\Theta_r}}. \tag{B.10}$$

B.2 Vibrational Distribution

The equation for the energy of a vibrational state v relative to the ground state v=0 is

$$E_v = hcvw_e, \tag{B.11}$$

where w_e is the first term vibrational constant. The degeneracy g_v is equal to one. The vibrational partition function

$$Z_{vib}(T) = \sum_v g_v e^{\frac{-E_v}{k_BT}} \tag{B.12}$$

can be expressed as

$$Z_{vib}(T) = \sum_v e^{\frac{-hcvw_e}{k_BT}}. \tag{B.13}$$

The partition function can be further simplified by substituting the characteric vibrational temperature Θ_v into Equation (B.13). Θ_v is

$$\Theta_v = \frac{hv}{k_B}. \tag{B.14}$$

For I_2, Θ_v is approximately 308.62 K. Substituting into Equation (B.13), we obtain

$$Z_{vib}(T) = \sum_v e^{\frac{-\Theta_v v}{T}}, \tag{B.15}$$

and by using a convergent geometric series, Equation (B.15) becomes

$$Z_{vib} = (1 - e^{\frac{-\Theta_v}{T}})^{-1}. \tag{B.16}$$

As a result, the Boltzmann fraction for vibrational levels in Equation (B.1) becomes

$$\frac{N_v}{N} = \frac{e^{\frac{-hcvw_e}{k_b T}}}{(1 - e^{\frac{-\Theta_v}{T}})^{-1}}. \tag{B.17}$$

B.3   Electronic Distribution

For I_2, the ground electronic state energy is zero, which in turn causes Equation (B.1) to be equal to one. The energy of the first electronic state of I_2 is 15769.01 cm$^-$1, which is sufficiently high enough to drive the exponential term to 0 until very high temperatures are reached, at which point diatomic I_2 would likely have dissociated. Equation (B.1) then reduces to one.

B.4   Nuclear Spin

The quantized spin of a nucleus about it's own axis can serve to alter the degeneracies of rotational states through a coupling between molecular spin and nuclear rotation. The nuclear partition function is

$$Z_{nuc} = \prod_{n=1}^{L}(2I_n + 1), \tag{B.18}$$

where L is the number of atoms, and I_n is the nuclear spin quantum number. For I_2, I is equal to 5/2. The nuclear degeneracy term is

$$g_{nuc} = \prod_{m=1}^{M} (2I_m + 1)^2 \pm \prod_{m=1}^{M} (2I_m + 1), \qquad \text{(B.19)}$$

where m refers to the individual atom. For I_2, which follows Bose statistics, an even rotational quantum number will result in a $+$ and an odd rotational quantum number will result in a $-$ for the $\pm$ dependent product. Since the nuclear energy term is high,

$$\frac{N_{nuc}}{N} = \frac{g_{nuc}}{6}. \qquad \text{(B.20)}$$

Typically the affect of nuclear spin is multiplied with the rotational terms to create a corrected rotational degeneracy and a corrected rotational partition function.

B.5 Modeling

By multiplying Equations (B.10) and (B.17) together, the fractional population of total molecules in a discrete vibrational and rotational levels can be determined. Figure B.1 shows the result of calculating the populations of the ground states in the R134(36,0) and P83(33,0) used during the wavelength tuning calibrations used in this work.
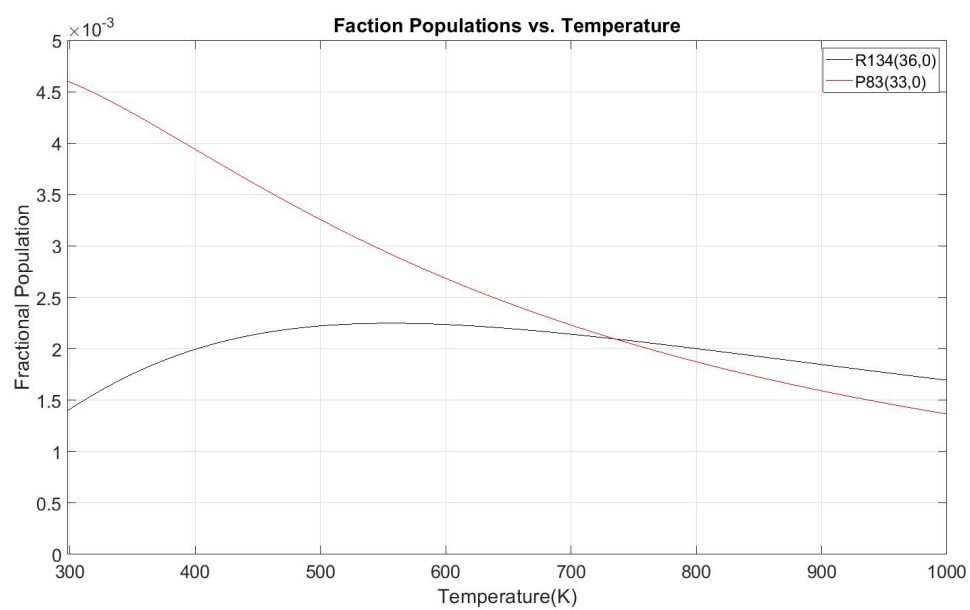
Fig. B.1. Boltzmann Fraction Calculations